# Impacts of waves and sea states on air-sea momentum flux in the Northwest Tropical Atlantic Ocean: parameterization and wave coupled climate modeling

Cesar Sauvage<sup>1</sup>, Hyodae Seo<sup>1</sup>, Carol Anne Clayson<sup>1</sup>, and James B Edson<sup>1</sup>

<sup>1</sup>Woods Hole Oceanographic Institution

November 28, 2022

#### Abstract

In winter, the Northwest Tropical Atlantic Ocean can be characterized by various regimes of interactions among ocean current, surface wind, and wind waves, which are critical for accurately describing surface wind stress. In this work, coupled waveocean-atmosphere model simulations are conducted using two different wave roughness parameterizations within COARE3.5, including one that relies solely on wind speed and another that uses wave age and wave slope as inputs. Comparisons with the directly measured momentum fluxes during the ATOMIC/EUREC4A experiments in winter 2020 show that, for sea states dominated by short wind waves under moderate to strong winds, the wave-based formulation increases the surface roughness length by  $40\$ % compared to the wind-speed-based approach. For sea states dominated by remotely generated swells under moderate to strong wind intensity, the wave-based formulation predicts significantly lower roughness length and surface stress (~20%), resulting in increased near-surface wind speed above the constant flux layer (~5%). Further investigation of the mixed sea states in the model and data indicates that the impact of swell on wind stress is over-emphasized in the COARE3.5 wavebased formulation, especially under moderate wind regimes. Various approaches are explored to alleviate this deficiency by either introducing directional alignment between wind and waves or using the mean wave period instead of the wave period corresponding to the spectral peak to compute the wave age.

# Impacts of waves and sea states on air-sea momentum flux in the Northwest Tropical Atlantic Ocean: parameterization and wave coupled climate modeling

César Sauvage<sup>1</sup>, Hyodae Seo<sup>1</sup>, Carol Anne Clayson<sup>1</sup>, and James B. Edson<sup>1</sup>.

 $^1 \rm Woods$  Hole Oceanographic Institution, Woods Hole, Massachusetts, USA

# Key Points:

4

5

6

9

10

11

7	•	Surface stress at moderate to high winds is dominated by short wind waves.
8	•	COARE3.5 wave based formulation overestimates swell impact on the surface

- stress in mixed sea conditions.
- Using the mean wave period or including the directional alignment between wind and wave in COARE3.5 alleviates this issue.

Corresponding author: César Sauvage, csauvage@whoi.edu

#### 12 Abstract

In winter, the Northwest Tropical Atlantic Ocean can be characterized by vari-13 ous regimes of interactions among ocean current, surface wind, and wind waves, 14 which are critical for accurately describing surface wind stress. In this work, coupled 15 wave-ocean-atmosphere model simulations are conducted using two different wave 16 roughness parameterizations within COARE3.5, including one that relies solely on 17 wind speed and another that uses wave age and wave slope as inputs. Comparisons 18 with the directly measured momentum fluxes during the ATOMIC/EUREC<sup>4</sup>A ex-19 periments in winter 2020 show that, for sea states dominated by short wind waves 20 under moderate to strong winds, the wave-based formulation increases the surface 21 roughness length by 40% compared to the wind-speed-based approach. For sea 22 states dominated by remotely generated swells under moderate to strong wind in-23 tensity, the wave-based formulation predicts significantly lower roughness length 24 and surface stress ( $\approx 20\%$ ), resulting in increased near-surface wind speed above 25 the constant flux layer ( $\approx 5\%$ ). Further investigation of the mixed sea states in the 26 model and data indicates that the impact of swell on wind stress is over-emphasized 27 in the COARE3.5 wave-based formulation, especially under moderate wind regimes. 28 Various approaches are explored to alleviate this deficiency by either introducing di-29 rectional alignment between wind and waves or using the mean wave period instead 30 of the wave period corresponding to the spectral peak to compute the wave age. 31

#### <sup>32</sup> Plain Language Summary

Accurately understanding and describing air-sea interactions is critical for 33 weather forecast and regional climate. In this work, we use numerical experiments 34 with and without taking into account the ocean waves to describe air-sea interac-35 tions. Most of the momentum exchange between the ocean and the atmosphere is 36 done through locally wind-generated waves, however remotely generated waves, such 37 as swells, can also interfere in these air-sea interaction. Comparisons with observa-38 tions made during the ATOMIC/EUREC<sup>4</sup>A field campaigns in winter 2020 show in 39 particular that our numerical experiment overestimated the impact of the swell on 40 the atmosphere. Various approaches are explored here to alleviate this deficiency, 41 one of those being the introduction of the effect of the alignment between wind and 42 waves. 43

#### 44 1 Introduction

Over the ocean, most of the momentum, heat, and mass exchanges with the at-45 mosphere are supported by short wind-waves on spatial scales of O(0.1-10m). These 46 wind-waves enhance the surface drag and roughness at the air-sea interface, thereby 47 increasing the wind stress. The wind stress is coupled with the planetary boundary 48 layer (PBL) processes in the atmosphere, modifying the kinematic and thermody-49 namic profiles in this lowest part of the atmosphere (Janssen, 1989; Moon et al., 50 2004). In addition to locally generated wind-waves, the sea state is also influenced 51 by the remotely generated swell, especially in the lower latitudes, whose propagation 52 direction is often uncorrelated with local winds. The fast-propagating swell wave 53 that is strongly misaligned with or outruns the local wind can be a conduit for up-54 ward momentum and energy transfer from waves to the wind, forming a wave-driven 55 low-level jet (e.g., Harris, 1966; Sullivan et al., 2008; Hanley & Belcher, 2008) and 56 dissipating the swell waves (Donelan, 1999; Kahma et al., 2016; Liu et al., 2017). 57

In the atmospheric models, the wind stress over the oceans is parameterized in the surface-layer scheme using bulk formulas, such as the Coupled Ocean-Atmosphere Response Experiment (COARE, Fairall et al., 1996, 2003; Edson et al., 2013). If no coincident wave fields are available, COARE parameterizes the wave

roughness length  $(z_0)$  using wind speeds only. In this study, this approach will be 62 referred to as the wind-speed-dependent formulation (WSDF). Since wind and wind-63 waves are in near-equilibrium in many cases over the extratropical open oceans, the 64 COARE's WSDF accurately parameterizes the surface roughness and thereby the 65 surface stress (Edson et al., 2013). However, under low-wind regimes, especially in 66 the tropics such as our study region, where longer waves and swell may not be in 67 equilibrium with the local winds, wind speed alone is insufficient to describe the 68 wave impact on the surface stress and surface roughness. To improve estimates of 69 the fluxes under these conditions, "wave-based" formulations exist in many bulk flux 70 algorithms that model  $z_0$  as a function of wave age or wave age/slope (e.g., Taylor 71 & Yelland, 2001; Oost et al., 2002; Drennan et al., 2003; Edson et al., 2013; Sauvage 72 et al., 2020). As there are increasing interests and opportunities to incorporate the 73 wave effects on surface fluxes in numerical models, such wave-based formulations 74 (WBF) in bulk formulas will likely be adopted more in such models. It is, then, 75 imperative to understand the challenges and deficiencies in current WBFs and offer 76 possible revisions to the formulations for air-sea fluxes with increased accuracy. The 77 goal of this paper is to enhance a regime-based understanding of wave-wind interac-78 tions via detailed validation of the parameterized air-sea flux from high-resolution 79 coupled model simulations against directly measured air-sea fluxes. 80

This study focuses on air-sea momentum flux during the ATOMIC/EUREC<sup>4</sup>A 81 field campaign. The ATOMIC (Atlantic Tradewind Ocean-Atmosphere Mesoscale 82 Interaction Campaign) is the U.S. complement to the European field campaign, 83 EUREC<sup>4</sup>A (ElUcidating the RolE of Cloud–Circulation Coupling in ClimAte, 84 Stevens et al., 2021), both of which took place in the Northwest Tropical Atlantic 85 Ocean in January-February 2020 (Figure 1). The primary objective of this study is 86 to determine how well the current WBF in an advanced bulk flux algorithm such as 87 COARE3.5 reproduces the observed wind stress in the mixed sea conditions com-88 pared to the WSDF. By exploiting the fully-coupled ocean-atmosphere-wave model 89 simulations and extensive analyses of the in situ observational datasets, we will at-90 tempt to explain the causes for discrepancies between simulated and measured wind 91 stresses. Our results indicate that the current COARE3.5 WBF underestimates  $z_0$ 92 and wind stress, particularly over the mixed sea state. We will show that this is due 93 to either a missing physics of the wave-wind interaction or using an inappropriate 94 wave input parameter to describe the mixed sea condition. This will rectify these 95 problems by accounting for the missing physics or refining the wave input parame-96 ters in the formulations used in the current COARE3.5 WBF. 97

The paper is organized as follows. Section 2 describes the technical details 98 of the latest  $z_0$  formulation in COARE3.5. Sections 2b,c discuss the fully coupled 99 ocean-atmosphere-wave modeling system used in the investigation, followed by the 100 details on the experimental design and observational datasets in Section 2d and Sec-101 tion 2f, respectively. The wave impact on  $z_0$ , wind stress, and low-level winds are 102 discussed in a case study investigation in Section 3. Section 4 provides an in-depth 103 comparison of the parameterized momentum flux against the direct measurements, 104 identifying the areas and regimes for further improvement. In section 5, possible 105 approaches are proposed and tested to alleviate the biases. Section 6 provides a 106 summary and discussion. 107

### <sup>108</sup> 2 Air-sea flux parameterization and coupled model

The interaction across the air-sea interface determines the turbulent exchanges of heat, moisture, and momentum, which are typically parameterized in atmospheric, ocean, and wave models using bulk aerodynamic formulas. This section provides a brief overview of the wave-mediated momentum flux implemented in

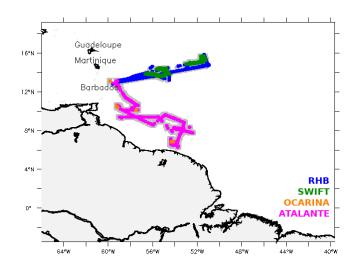


Figure 1. Tracks of the different platforms measuring surface stress (see more details in Section 2.5). The gray area denotes where the model outputs are sampled along the tracks of observations.

the Coupled Ocean-Atmosphere Response Experiment parameterization (COARE,
Fairall et al., 1996, 2003; Edson et al., 2013).

#### 115 2.1 Roughness length and momentum flux in COARE3.5

<sup>116</sup> The along wind stress in the COARE framework is defined as:

$$\tau = \rho C_D(z, z_0, \psi_m) U_r(z) S_r(z) = \rho u_*^2, \tag{1}$$

where  $\rho_a$  is the air density,  $U_r(z)$  is the magnitude of the along-wind component of the wind vector,  $S_r(z)$  is the scalar wind speed, where the subscript r denotes relative to the ocean surface; and  $u_*$  the friction velocity.  $C_D$  is the drag coefficient defined as:

$$C_D(z, z_0, \psi_m) = \left[\frac{\kappa}{\ln(z/z_0) - \psi_m(\zeta)}\right]^2,\tag{2}$$

<sup>121</sup> where  $\kappa$  is the von Kármán constant,  $\psi_m(\zeta)$  is an empirical function of at-<sup>122</sup> mospheric stability,  $\zeta$  is the z/L ratio with L the Obukhov length and z the height <sup>123</sup> above the surface (Fairall et al., 1996). The surface roughness length  $z_0$  is parame-<sup>124</sup> terized in COARE3.5 as the sum of two terms:

$$z_0 = z_0^{smooth} + z_0^{rough},\tag{3}$$

where  $z_0^{smooth}$  and  $z_0^{rough}$  represent the smooth and rough flow components of  $z_0$ , respectively (Edson et al., 2013). The smooth flow component is parameterized as

$$z_0^{smooth} = \gamma \frac{\nu}{u_*},\tag{4}$$

<sup>128</sup> where  $\gamma$  is the roughness Reynolds number for smooth flow, set to be con-<sup>129</sup> stant at 0.11 based on laboratory experiments, and  $\nu$  is the kinematic viscos-<sup>130</sup> ity. For smooth flow, the wind stress is mainly supported by viscous stress where <sup>131</sup>  $z_0 \approx z_0^{smooth}$ .

The rough part of the roughness length,  $z_0^{rough}$ , is meant to parameterize the wind-driven gravity waves that support most of the stress above approximately 5  $ms^{-1}$  when the sea becomes aerodynamically rough. This component of the roughness is formulated currently in several ways in COARE3.5. The simplest and the most broadly used way is to parameterize it as a function of wind speed only. The so-called wind speed dependent formulation without explicit wave and sea states inputs estimates  $z_0^{rough}$  using the Charnock's relation (Charnock, 1955):

$$z_0^{rough} = \frac{\alpha_{ch} u_*^2}{g},\tag{5}$$

where g is the acceleration of gravity and  $\alpha_{CH}$  is the Charnock coefficient that is dependent only on wind speed. COARE3.5 formulates  $\alpha_{CH}$  as

$$\alpha_{ch} = mU_{r10N} + b,\tag{6}$$

where  $U_{r10N}$  is the 10-m wind speed relative to the sea surface under neutral conditions (Edson et al., 2013, Appendix) and coefficients m = 0.0017 and b = -0.005 (Edson et al., 2014). Hereafter,  $U_{r10N}$  is defined such as:

$$U_{r10N} = \frac{u_*}{\kappa} ln(10/z_0),$$
(7)

The coefficients m, and b in Eq. 6, have been determined to fit the average data used in COARE3.5 over wind speeds between 5 and 18  $ms^{-1}$ . If wind speed is below 5  $ms^{-1}$ , the surface roughness is mainly determined by  $z_{smooth}$  in Eq. 4. For wind speeds greater than 18  $ms^{-1}$ , COARE3.5 fixes the value of the Charnock coefficient to its value at 18  $ms^{-1}$ . Note, however, that although  $\alpha_{CH}$  is fixed above 18  $ms^{-1}$ ,  $z_0^{rough}$ ,  $C_D$  and  $\tau$  all continue to increase with the wind speed, just at a lower rate.

An alternative way to define  $z_0^{rough}$  in COARE3.5 is to use the so-called wavebased formulation (WBF), which requires contemporary information about the wave field and its state of development, such as significant wave height  $(H_s)$  and phase speed of the dominant waves  $(c_p)$ . Two WBFs are currently available in COARE3.5, one that uses the wave age only and another that uses both the wave age and wave steepness. In the second form, which is explored in this study in great detail,  $z_0^{rough}$ is expressed as

$$z_0^{rough} = H_s D(\frac{u_*}{c_p})^B,\tag{8}$$

where  $u_*/c_p$  is the inverse wave age based on the friction velocity, and D and B are numerical constants given by D = 0.09 and B = 2 in Edson et al. (2013). Hereafter, we will use a definition of wave age based on the ratio of the phase speed of the waves at the spectral peak over the surface wind speed at 10 m defined as

$$\chi = \frac{c_p}{U_{10}}.\tag{9}$$

The wave age is used to describe the state of development of the wave field. 162 For example, a wave age close to 1.2 represents a fully developed sea when the sur-163 face waves and stress are largely in equilibrium (e.g., Phillips, 1985), in which the 164 rate that wind does work on the surface waves is balanced by the dissipation rate of 165 breaking waves (microbreakers and whitecaps) and nonlinear wave-wave interactions 166 (e.g., Csanady & Gibson, 2001). Wave ages under 1 are associated with developing 167 seas and young waves, while wave ages well above 1.2 describe decaying seas and 168 swell. It should be noted that in the current COARE3.5,  $c_p$  is defined using the peak 169 period of the waves,  $T_p$ , in deep water such that: 170

$$c_p = g \frac{T_p}{2\pi}.$$
(10)

In Section 3, we will examine the sensitivity of the estimated momentum flux based on the current COARE3.5 algorithm. Guided by comparison to the observations in Section 4, we will then explore the impacts of revised COARE3.5 WBF in Section 5.

#### 2.2 SCOAR regional coupled model system

We use the Scripps Coupled Ocean-Atmosphere Regional (SCOAR) model 176 (Seo et al., 2007, 2021), which couples the Weather Research and Forecast (WRF. 177 Skamarock et al., 2008) Model to the Regional Ocean Modeling System (ROMS, 178 Shchepetkin & McWilliams, 2005) via the COARE3.5 bulk flux algorithm (Fairall 179 et al., 1996, 2003; Edson et al., 2013). In the absence of wave coupling, ROMS 180 is driven by the surface heat flux  $(Q_{NET})$ , momentum flux  $(\tau)$ , and freshwater 181 flux  $(Q_{FW})$  computed from the wind speed-only formulation in COARE3.5 imple-182 mented in WRF. In turn, ROMS inputs SST and surface current vectors  $(U_s)$  to the 183 COARE3.5 to compute the surface fluxes (Figure 2). 184

#### 185 2.3 Wave coupling in SCOAR

175

Taking advantage of the COARE's WBF, this study implemented the cou-186 pling of the third-generation spectral wave model WaveWatch-III (WW3 Tolman 187 et al., 2002; The WAVEWATCH III Development Group, 2016) into the SCOAR. 188 The centerpiece of the model coupling is the COARE3.5 implemented in the surface 189 layer scheme in WRF to compute the air-sea fluxes. In this study, we use the Mellor-190 Yamada-Nakanishi-Niino (MYNN) surface layer scheme (Nakanishi & Niino, 2009; 191 Jiménez et al., 2012), which over the ocean grid points computes the surface fluxes 192 using the COARE3.5 WBF. WW3 is forced by the surface wind  $(U_{10})$  from WRF 193 and ocean current  $(U_s)$  from ROMS. WW3 then returns the significant wave height 194  $(H_s)$  and the phase speed of the dominant waves  $(c_p)$  determined based on  $T_p$  (Eq. 195 10) to the MYNN surface layer scheme. In lieu of  $c_p$ , WW3 can alternatively send 196 the mean phase speed  $(c_m)$  and peak wave direction (Section 5). Spatially varying 197 Charnock coefficients  $(\alpha_{CH})$  are then updated to parameterize the surface roughness 198 length  $(z_0)$  as a function of dominant wave age  $(\chi)$  and wave steepness (Eq. 8). For 199 this to work in WRF, the MYNN surface layer scheme has been modified to allow 200 ingestion of wave age and significant wave height  $(H_s)$  from WW3. The MYNN PBL 201 scheme (Nakanishi & Niino, 2004, 2006) is coupled to this modified surface layer 202 scheme, allowing for the adjusted  $z_0$ , wind stress  $(\tau)$ , and latent  $(Q_{LH})$  and sensi-203 ble  $(Q_{SH})$  heat fluxes to influence the kinematic and thermodynamics processes in 204 the PBL. The surface layer scheme has also been modified to take the ocean sur-205 face currents  $(U_s)$  from ROMS to compute the relative wind and thus represent 206 wind-current interaction. This so-called relative wind effect is represented in all 207 simulations analyzed here. 208

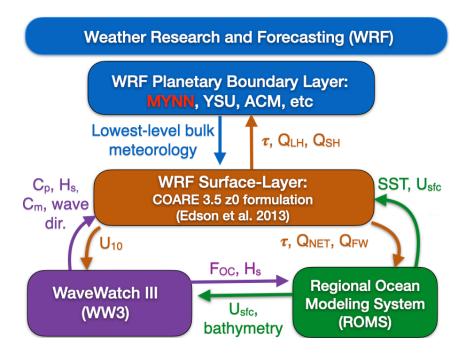


**Figure 2.** SCOAR WRF-ROMS-WW3 coupling flowchart. See the text for the variable names that are exchanged across the model components.

#### 2.4 Experiments

209

In WRF, the deep cumulus convection is represented through the Multi-scale 210 Kain-Fritsch scheme (Zheng et al., 2016), the cloud micro-physics by the WRF 211 single-moment 6-class scheme (Hong & Lim, 2006). The Goddard radiation scheme 212 (Chou & Suarez, 1999) is used for shortwave and longwave radiation. The land 213 surface process is treated with the Noah land surface model (F. Chen & Dudhia, 214 2001). In ROMS, the KPP (K profile parameterization) scheme (Large et al., 1994) 215 determines vertical eddy viscosity and diffusivity. The vertical grid in ROMS is 216 stretched to enhance the resolutions near the surface and the bottom, using the so-217 called stretching parameters of  $\theta_s = 7.0$ ,  $\theta_b = 2.0$ , and  $h_{cline} = 300$  m. In WW3, the 218 set of parameterizations from Ardhuin et al. (2010) is used, including swell dissipa-219 tion scheme (Ardhuin et al., 2009). Nonlinear wave–wave interactions are computed 220 using the discrete interaction approximation (Hasselmann et al., 1985). Reflection 221 by shorelines are enabled through Ardhuin and Roland (2012) scheme. The depth-222 induced breaking is based on Battjes and Janssen (1978), and the bottom friction 223 formulation follows Ardhuin et al. (2003). 224

The model domain covers the Northwest Tropical Atlantic Ocean (Figure 3). The horizontal resolutions in WRF, ROMS, and WW3 are identical 10 km, with matching grids and land-sea masks. ROMS (WRF) is run with a stretched vertical grid with a total of 30 (33) vertical levels, with approximately 10 layers in the upper 150 m (below 1300 m). The model coupling is activated every 3 hours to account for the diurnal cycle.

A set of coupled model simulations presented in Section 4 is run for 6 months (November 1, 2019 to May 1, 2020), covering the ATOMIC/EUREC<sup>4</sup>A period, with a specific aim to compare with the measurements. In these simulations, the WRF model is initialized and driven by 3-hourly ERA5 global reanalysis at 0.25° resolution (Hersbach et al., 2018a, 2018b), ROMS by the daily MERCATOR International

global reanalysis at  $1/12^{\circ}$  resolution (Lellouche et al., 2018), and WW3 by seven 236 spectral points obtained from the global  $1/2^{\circ}$  resolution WW3 simulations (Rascle 237 & Ardhuin, 2013). The initial conditions for ROMS and WW3 were obtained from 238 the respective ROMS-only and WW3-only spin-up simulations forced by ERA5 at-239 mospheric forcing (starting from January 1, 2019). In ROMS, the tidal forcing is 240 obtained using the Oregon State University Tidal Prediction Software (Egbert & 241 Erofeeva, 2002) and applied as a 2-D open boundary condition by prescribing the 242 tidal period, elevation amplitude, current phase angle, current inclination angle, the 243 minimum and maximum tidal current, and ellipse semi-minor axes for 13 major tidal 244 constituents. Daily climatology estimates of the Amazon and River and Orinoco 245 River discharges are obtained from the Observatory Service SO-HyBAM database 246 (https://hybam.obs-mip.fr/), which are prescribed as point sources close to the river 247 mouths in our grid. 248

The second set of simulations presented in Section 3 is identical to that of the 249 6-month-long simulations, except that WRF, ROMS, and WW3 are initialized from 250 respectively 3-hourly ERA5 global reanalysis for the atmosphere and ROMS-only 251 and WW3-only spin-up simulations for the ocean and waves as described above 252 and run on a particular day (January 8, 2020) as a case study investigation. The 253 motivation for the short simulations with the identical initial condition is to isolate 254 the immediate impacts on  $z_0$  and  $\tau$  before the coupled feedback begins to alter the 255 state variables. One could use the identical input state variables to estimate the 256 air-sea fluxes offline using different COARE formulations. This yields similar results 257 (not shown), indicating that the difference we show in Section 3 is not due to the 258 difference in state variables but due to the formulation difference. One notable ad-259 vantage to use the fully coupled model simulation is that it allows for evaluating the 260 wind response beyond the surface layer (e.g., Figure 6c), and potentially large-scale 261 feedback effects via the coupling. 262

Experiments	$z_0$ parameterization	Relative wind	Wave period	misaligned wave
WSDF	wind speed [Eq. 5]	yes	/	/
WBF	wave age $+$ wave steepness [Eq. 8]	yes	$T_p$	no
$WBF_{-}\theta$	wave age $+$ wave steepness [Eq. 11]	yes	$T_p$	yes
$WBF_T_m$	wave age $+$ wave steepness [Eq. 12]	yes	$T_m$	no

Table 1. Summary of the different SCOAR experiments.

Table 1 summarizes 4 experiments conducted in this study, where the only 263 difference is in the way  $z_0$  is parameterized in COARE3.5. In the first run (dubbed 264 WSDF), the wind speed only formulation is used (hence, only WRF-ROMS cou-265 pling), while in the second run (WBF), the default wave-based formulation is used 266 (WRF-ROMS-WW3). These two runs are examined in detail in Sections 3-4. Two 267 additional runs, discussed in Section 5, are conducted with a modified wave-based 268 formulation. WBF  $\theta$  takes into account the directional misalignment between wind 269 and wave, while WBF<sub> $-T_m$ </sub> modifies the definition of wave age based on mean wave 270 period rather than the peak wave period. 271

All simulations used in this study produce output every 3h. Since this output interval is much coarser than the typical sampling intervals used in the observations (Section 2e), there is inevitable inconsistency in sampling frequency and the number of samples between the model and data. We attempt to increase the model sample size and capture more spatio-temporal variability by sampling a slightly broader region of the model domain encompassing the particular observational tracks (grayareas in Figure 1a).

279

#### 2.5 ATOMIC/EUREC<sup>4</sup>A observations

This study will exploit direct and indirect measurements of momentum 280 fluxes and relevant wave fields from various platforms deployed during the 281 ATOMIC/EUREC<sup>4</sup>A experiment. Figure 1 shows the tracks of the different obser-282 vational platforms, including the R/V Ronald H. Brown (RHB, Quinn et al., 2021; 283 Thompson et al., 2021), R/V ATALANTE (Bourras, Gevskens, et al., 2020), SWIFT 284 drifters (Surface Wave Instrument Float with Tracking, Thomson, 2012; Thomson 285 et al., 2019, 2021), and OCARINA (Ocean Coupled to Atmosphere, Research at 286 the Interface with a Novel Autonomous platform, (Bourras, Branger, et al., 2020) 287 surface naval drone. The RHB provides direct momentum flux measurements every 288 10 minutes in the so-called "Tradewind Alley" region from January 9 to February 289 13, 2020. The SWIFT drifters were deployed from the RHB, from which the hourly 290 stress can be estimated using the equilibrium frequency range in the wave spectrum 291 (Iyer et al., 2021). The R/V ATALANTE measured the wind stress mostly in the 292 "Eddy Boulevard" region based on the inertial dissipation method. OCARINA was 293 deployed from the R/V ATALANTE from January 25 to February 17, 2020 (with 294 some discontinuity), providing direct wind stress measurements every minute. 295

#### (a) 10-m wind speed and direction

(b) Wave age and wave peak direction

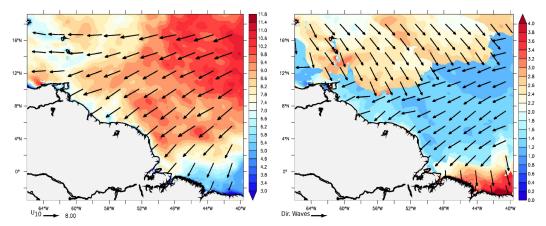


**Figure 3.** Snapshots of (a) 10-m wind speeds (shading) and direction (arrows) and (b) peak wave age (shading) and wave peak direction (arrows) on January 8, 2020 at 0600 UTC.

# <sup>296</sup> 3 Impacts of wave and sea state: a case study

To demonstrate the immediate effect of including waves on  $z_0$  and  $\tau$  in the COARE3.5 using a coupled model, we will first compare the simulation results close to the initial condition. By doing so, the input state variables into the bulk formula remain largely identical, and any differences in simulated  $z_0$  and  $\tau$  can be attributed to the difference in the formulations. From this set of experiments, we will compare the results 3 hours after the initial condition.

The sea state and wind fields on January 8, 2020 at 0600 UTC, shown in Figure 3a, illustrate the archetypal synoptic condition observed in this region during the boreal winter. Much of the domain was under the influence of northeasterly trade

winds with wind speeds of 7-13  $ms^{-1}$ , while the northern and southeastern parts of 306 the domain experienced much weaker  $(<7 m s^{-1})$  easterly and northerly winds, re-307 spectively. Figure 3b shows the corresponding wave age and peak wave direction. In 308 the Tradewind Alley region, surface waves were predominantly downwind with rela-309 tively small wave age, indicating the developing seas with young waves. Away from 310 the trade winds, especially in the northern part of the domain, the wave vectors are 311 generally misaligned with the local wind vectors, and the wave age is high, indicative 312 of the swell-dominated sea state. 313

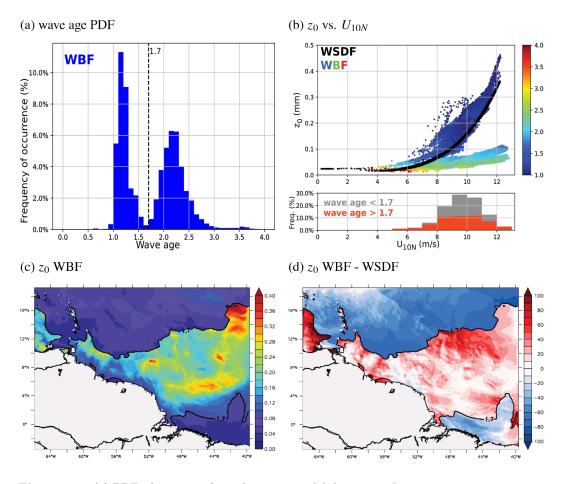


Figure 4. (a) PDF of wave age from the entire model domain on January 8, 2020 at 0600 UTC. The dotted vertical line denotes the wave age of 1.7, below (above) which the sea state is characterized as developing, equilibrium and slightly old waves (mature waves and swell). The upper panel of (b) is a scatter plot of  $z_0$  (mm) vs.  $U_{10N}$  ( $ms^{-1}$ ).  $z_0$  from WSDF is shown in black, while  $z_0$  from WBF is color-coded to denote the corresponding wave age. The stacked PDFs of  $U_{10N}$  in the lower panel of (b) are constructed when wave age is above 1.7 (red) and below 1.7 (gray). (c) A map of  $z_0$  from WBF, superposed with a contour of wave age = 1.7. (d) A map of percentage difference of  $z_0$  between WBF and WSDF

To illustrate sea state distribution differently, Figure 4a shows the probability density function (PDF) of wave age for the same period. Two distinct peaks of wave age stand out clearly. The first peak resides on wave age between 0.8 and 1.7, corresponding to developing (young) waves to fully developed (mature) seas. The secondary peak is found over a wide range of wave age greater than 1.7, reaching up to 4-5, the latter representing swell. Indeed, the fact that there is a gap at 1.7

strongly suggests that the older waves are swell, as opposed to the continuum of 320 longer/older wind waves. Thus, in this case, we choose to use 1.7 as a threshold for 321 fully developed seas and not the usual value of 1.2 which is what you might expect 322 for wind waves dominated region. As a matter of fact, this swell-dominated sea state 323 is frequently observed in the ATOMIC region in the boreal winter (e.g., Semedo et 324 al., 2011; Jiang & Chen, 2013). Indeed, if considering the entire month of January 325 2020 in our simulations, we find that wave ages greater than 2 occur more than 60%326 of the time in this domain. 327

328 Figure 4b compares the  $z_0$  against wind speed from the WSDF (black) and WBF (color) runs for this period.  $z_0$  from WBF is color-coded to denote the cor-329 responding wave age. The bottom panel shows stacked PDFs of 10-m wind speeds 330 from WBF, with the red (gray) parts representing the proportion of wind associ-331 ated with wage age over (under) 1.7. The WSDF in COARE3.5 assumes young seas 332 under moderate to high winds, and hence the parameterized  $z_0$  (black) obeys the 333 well-known quadratic dependence on wind speed. The surface roughness  $z_0$  from 334 WSDF shows less scatter because it is based solely on wind speed. 335

In contrast, WBF captures the two wave age-dependent regimes of  $z_0$  that appear distinct from WSDF. The first is the cluster of  $z_0$ , which increases more rapidly with wind speed than WSDF  $z_0$  and occurs over 4-12  $ms^{-1}$ . The wave age of this cluster (shading) is typically less than 1.7, corresponding to the first wave age peak in Figure 4a of small-scale young waves. Thus, the developing and equilibrium waves under these wind speeds and wave age conditions increase  $z_0$  in WBF compared to WSDF.

The second cluster indicates significantly decreased  $z_0$  in WBF with wind 343 speed up to  $12 m s^{-1}$ . This cluster can be further split into two different wind speed 344 groups, under and above 8  $ms^{-1}$ , color-coded by the PDF of winds (Figure 4b). 345 Below 8  $ms^{-1}$  (red, weak winds), the wave age tends to be greater than 1.7, where 346 remotely generated swell appears to dominate the sea state. However, the wind 347 speeds under 8  $ms^{-1}$  account for less than 10% of the total wind speed data, and 348 thereby it has a relatively small impact on the space/time-averaged  $z_0$ . Indeed, 349 when averaged for wind speed below 8  $ms^{-1}$ , the percentage difference in  $z_0$  between 350 WSDF and WBF, defined as (WBF-WSDF/WSDF)\* 100, is only -1.7%. 351

During this day, most of the wind speed is above 8  $ms^{-1}$ . In addition to the 352 proportion of low wave age expected under this moderately high wind speed, we 353 also find an increased occurrence of large wave age, accounting for about 50% of 354 the data (Figure 4b). The co-existence of high wind and swell indicates a mixed 355 sea condition. In this case, when averaged over wind speed above 8  $ms^{-1}$ , the swell 356 impact appears much more significant, with  $z_0$  in WBF being 15.7% lower than 357 that in WSDF. The working hypothesis is that the use of the phase speed at the 358 spectral peak causes the WBF to assume that the swell is supporting most of the 359 stress; even under moderate winds. The strong impact of swell at moderate winds is 360 questionable and will be a focus of this investigation. 361

The spatial distribution of  $z_0$  from WBF is shown in Figure 4c. The  $z_0$  dif-362 ference between WBF and WSDF is shown in Figure 4d. As in Figure 4a,b, two 363 distinct regimes of  $z_0$  are readily apparent on the map, delineated sharply by the 364 contour of wave age 1.7 (black). In the first regime of increased  $z_0$  in WBF under 365 moderate to strong trade winds, the WBF predicts an increased  $z_0$  by on average 366  $\approx 50\%$  compared to WSDF. This increased  $z_0$  is expected as the WBF  $z_0$  formula-367 tion (Eq. 8) takes into account the effect of wave slope on the aerodynamic rough-368 ness of the sea surface. That is, Figure 5a, b show that wave slope under young 369 waves is higher, where the choppy sea surface increases  $z_0$ . Figure 5c,d shows the 370 angle ( $\theta$ ) between the wind direction and peak wave direction. If  $\theta = 0^{\circ}$ , wind and 371

waves are perfectly aligned, whereas  $\theta = 180^{\circ}$  means wind and waves are opposed. Under this wind/wave regime, the peak wave direction is largely downwind since  $\theta$  is generally less than 50°. This corroborates that these waves are young waves driven by local winds.

Figure 4d also shows the second regime of decreased  $z_0$  with the inclusion of 376 waves, especially in the northern part of the domain. In this region, the remotely 377 generated swell propagates into the domain through the northern boundary and 378 forms a sea state with the aerodynamically smooth sea surfaces (Figure 5a,b) and 379 with waves whose direction is strongly misaligned ( $\theta = 60 - 160^{\circ}$ ) with the local wind 380 (Figure 5c,d). In particular, the reduced  $z_0$  over swell persists under wind speed of 381 up to  $12 ms^{-1}$  (Figure 3a), despite the expectation that under such a high wind, the 382 wind-waves would still strongly increase the aerodynamic roughness and stress. 383

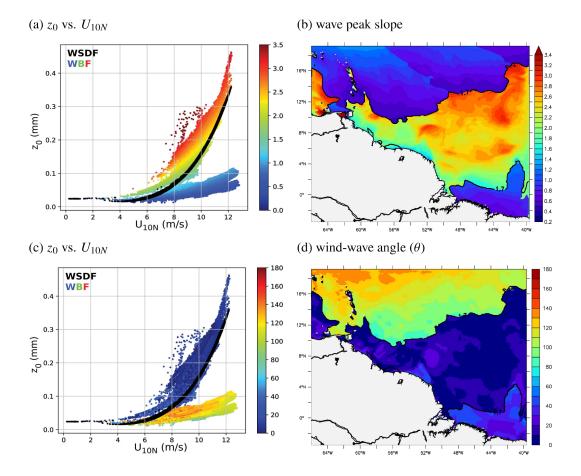


Figure 5. (a) Scatter plot of  $z_0$  (mm) vs.  $U_{10N}$  ( $ms^{-1}$ ) from WSDF in black and WBF colorcoded to denote the corresponding wave peak slope  $(10^{-2})$  defined as  $H_s/L_p$  where  $L_p$  is the peak wavelength. (b) A map of wave slope peak  $(10^{-2})$ , superposed with a contour of wave age = 1.7 on January 8, 2020 at 0600 UTC. (c,d) As in (a-b) except that colored scatters and shading denote the angle between the wind and wave directions ( $^{o}$ ).

384 385 386

387

388

Figure 6a,b compare the parameterized wind stress in WBF and WSDF. One can see from these plots a consistent difference in wind stress due to the inclusion of waves. Wind stress decreases sharply in wind speeds of 8-12  $ms^{-1}$  over the northerly swell where wave age >1.7. The percentage difference in wind stress magnitude exceeds 10%. Conversely, wind stress is increased in WBF by  $\approx 4\%$  over fully devel-

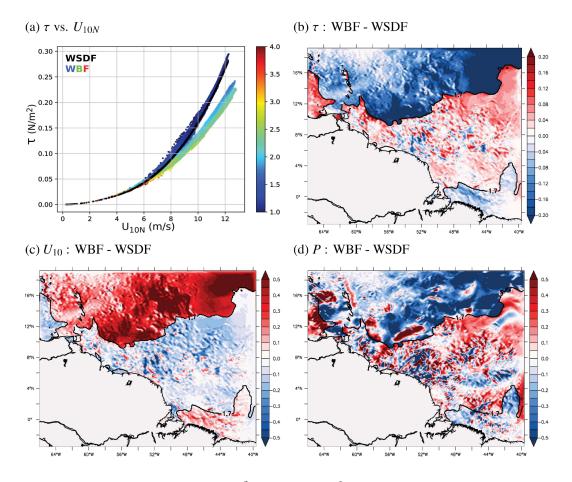


Figure 6. (a) Scatter plot of  $\tau$  (Nm<sup>-2</sup>) vs.  $U_{10N}$  ( $ms^{-1}$ ) from WSDF in black and WBF color-coded to denote the corresponding wave age. (b,c,d) Difference maps between WBF and WSDF of (b)  $\tau$  ( $10^{-1}$  Nm<sup>-2</sup>), (c)  $U_{10}$  ( $ms^{-1}$ ), and (d) wind work (P,  $10^{-5}m^3s^{-3}$ ) on January 8, 2020 at 0600 UTC, superposed with a contour of wave age = 1.7.

oped seas (wave age <1.7) and high winds, consistent with the increase in  $z_0$  there 389 (Figure 4c). By comparing to the direct momentum flux observations, we will deter-390 mine in Section 4 if such reduced  $z_0$  and  $\tau$  over swell conditions at moderate to high 391 wind speeds are consistent with the observations. As COARE3.5 does not consider 392 the misaligned waves with winds, these conditions may constitute a source of uncer-393 tainty in the parameterized  $z_0$  and  $\tau$  via COARE3.5 WBF. As for the large wave age 394 in the southeastern corner of the domain, it is concurrent with weaker winds (Figure 395 3a), and hence the assumptions about the swell under weaker wind seem valid in 396 this region. This leads to a small difference in  $z_0$  between WBF and WSDF. 397

The altered stress directly influences the low-level winds via the surface drag. 398 Here, we estimate the response in low-level winds at the lowest WRF model layer, 399 at about 27 m above the sea surface. Figure 6c shows that the low-level wind is 400 increased over the aerodynamically smooth sea surface due to swell by  $>0.5 ms^{-1}$ , 401 accounting for 5-20% of the wind speed in WBF. Although weaker than under swell 402 conditions, in the Tradewind Alley, where the stress in WSDF was enhanced over 403 the fully developed waves, the wind stress is increased by 5% and the wind speed is 404 decreased. 405

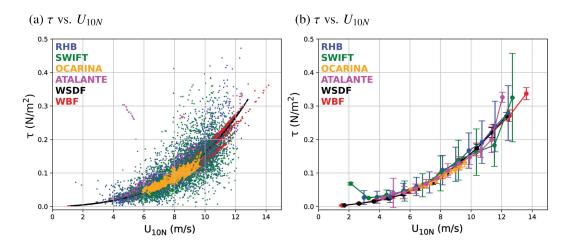


Figure 7. (a) Scatter plot comparing the two parameterized  $\tau$   $(Nm^{-2})$  using COARE3.5 WSDF (black) and WBF (red) against the various types of measurements of  $\tau$  (see Section 2e for a description of the various methodologies). (b) As in (a) except that measurements are bin-averaged with a wind speed bin-size of  $U_{10N} = 1 \text{ ms}^{-1}$ . The error bars represent  $\pm 1$  standard deviation.

<sup>406</sup> One relevant physical process that represents the air-sea momentum transfer <sup>407</sup> affecting the winds and surface currents, is the wind work (P),

$$P = \frac{1}{\rho_o} \left( \overline{u_s \tau_x} + \overline{v_s \tau_y} \right),\tag{11}$$

where  $(u_s, v_s)$  are the surface current vectors,  $(\tau_x, \tau_y)$  are the wind stress vec-408 tors, and the overbar denotes the time-average. When P is positive, the mechanical 409 work is done by the wind stress on the ocean surface currents, increasing the ocean 410 kinetic energy (e.g., Wunsch, 1998). When negative, it represents the diversion of 411 the ocean energy by the current to the wind, accelerating the low-level winds at 412 the expense of weakened surface currents (e.g., Renault et al., 2016, 2017; Seo et 413 al., 2019, 2021). Figure 6d shows the difference in P between WBF and WSDF for 414 this snapshot. The region of reduced  $\tau$  and increased low-level wind in the swell-415 dominated region is congruent with the region of the robust decrease in P, while the 416 opposite is true in the Tradewind Alley region. The difference in P mainly reflects 417 the changes in wind stress due to waves (Figure 6b). 418

## 4 Modeled and observed momentum fluxes during ATOMIC

<sup>420</sup> Determining whether or not the parameterized  $z_0$  and  $\tau$  with WBF represents <sup>421</sup> an improvement over WSDF requires a detailed comparison to direct covariance <sup>422</sup> stress measurements. In this section, we will compare the model simulation with <sup>423</sup> the observations during the EUREC<sup>4</sup>A/ATOMIC experiments to evaluate the ac-<sup>424</sup> curacy of the wave-based parameterized  $\tau$  and identify the regimes where further <sup>425</sup> improvements might be needed.

Figure 7a compares the two modeled stresses to the observations. All observations and the two model simulations display the quadratic relationship of wind stress with wind speed. RHB and SWIFT, sampling the stress mainly in the Tradewind Alley region, produce greater scatter compared to ATALANTE and OCARINA, which were deployed further south in the Eddy Boulevard region (1a). The significant departure from this curve in the Tradewind Alley region may reflect the greater uncertainties in determining  $\tau$  from these measurements. Between the model simulations, WBF produces a larger spread than WSDF, yet their averages at given wind speed are similar (Figure 7b). Overall, parameterized stresses by WSDF and WBF both agree well with the observations to within the observational errors during the campaign.

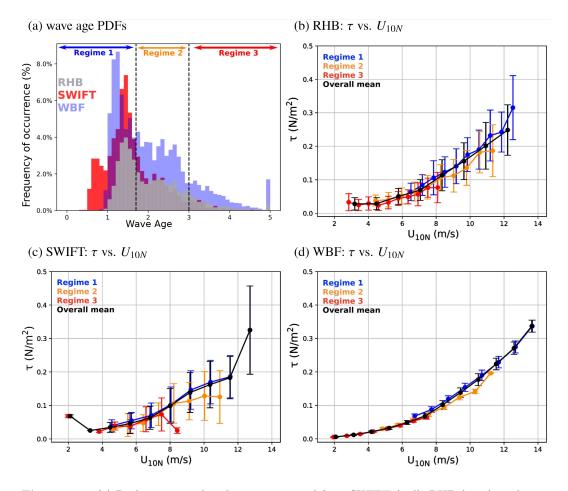


Figure 8. (a) Peak wave age distribution estimated from SWIFT (red), RHB (gray), and WBF (blue). Here, wave age is capped at 5. Three wave age regimes are defined: Regime 1 (blue) when wave age <1.7 denotes the young sea to fully developed sea, Regime 2 (orange) when wave age is between 1.7 and 3 indicates the mature to old sea, and Regime 3 (red) when wave age >3 represents the old sea and non-locally generated swell. (b-c) Binned scatter plots of  $\tau$  (Nm<sup>-2</sup>) vs.  $U_{10N}$  ( $ms^{-1}$ ), color-coded to show the three different wave age Regimes, with the bin-average of 1  $ms^{-1}$ . The mean of all wave ages is shown in black. (d) As in (b) and (c) except from the WBF run. Here WBF is sampled along-track of the RHB and SWIFT.

Figure 8a compares the histograms of the wave age from the WBF run to those from the SWIFT drifters and the RHB. It should be noted that in both the model and measurements, the wave age is estimated using the peak period  $(T_p)$ . The observations and model simulation show the bi-modal distribution of wave age as was seen from the snapshot case in Section 3 (Figure 4a), with the first peak near wave age 1.7 and the secondary, much broader, peak between 2.5-3. The SWIFT observations (in red) capture a higher occurrence of young waves than the RHB observations or the WBF simulation. WBF also features a fatter tail of the distribution
toward larger wave ages, indicating that the model overemphasizes the occurrences
of swell and decaying waves compared to these observed estimates.

Given the wave age distributions, we then divide the distribution into 3 dif-447 ferent "Regimes" to better understand the wave age-dependent  $z_0$ -wind speed and 448  $\tau$ -wind speed relationships. Regime 1 refers to young to fully developed seas, defined 449 as when wave age <1.7, while Regime 2 indicates the mature to old sea, including 450 mixed sea state, which is diagnosed as wave ages between 1.7 and 3. Finally, the old 451 452 sea and non-locally generated swell characterizes Regime 3 estimated as when wave age > 3. Note that these thresholds for different Regimes (e.g., the choice of peak 453 wave age of 3) are not unique, but can vary depending on specific conditions and 454 time periods under consideration. 455

The colored lines in Figures 8b and c show the bin-averaged surface stress 456 from the RHB and the SWIFT from the 3 Regimes. The black lines denote the 457 bin-averaged surface stress across all wave age regimes. Despite the significant error 458 bars, which represent  $\pm 1$  standard deviation, one can observe the consistent rela-459 tionship between the measured stress and the wind speed across different wave age. 460 For example, the measured stress over Regime 1 (blue) is higher than the overall 461 average (black) as the short-wind waves support the bulk of momentum exchanges. 462 In contrast, the stress over Regime 2 (orange) and Regime 3 (red) is lower than the 463 overall average, as the sea state is characterized by mixed and older seas. This sea state dependence of wind stress is also somewhat evident in the WBF simulation 465 (Figure 8d) despite the smaller error bars likely due to smaller number of samples in 466 the model, as discussed in Section 2d. 467

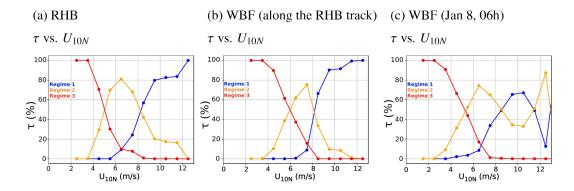
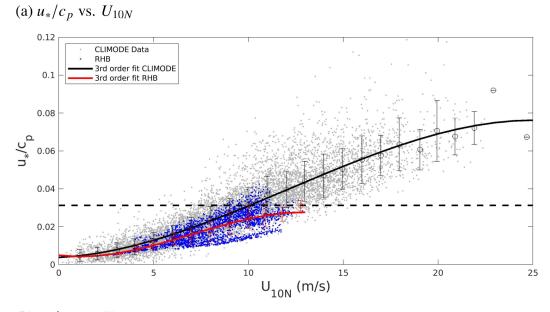
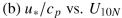


Figure 9. Percentage contribution of  $\tau$  (%) by the three different wave age Regime at a given wind speed (bin averaged every 1  $ms^{-1}$ ) from (a) RHB, (b) WBF sampled along the RHB track between January 9 and February 13, 2020 and (c) WBF sampled over the whole model domain on January 8, 2020 at 0600 UTC. The different colors denote the different wave age categories described in Figure 8.

To further quantify this relationship, Figure 9a shows the percentage of stress 468 supported by the different wave-age Regimes from the RHB observations, binned 469 over 1  $ms^{-1}$  intervals. Under 4  $ms^{-1}$  wind speeds, the surface stress is mainly 470 supported by Regime 3 (red), whereas above 8  $ms^{-1}$ , Regime 1 (blue) dominates 471 the contribution to the stress. Regime 2, which represents mixed sea conditions 472 (orange), mainly supports the surface stress at low to moderate wind speeds (4-8 473  $ms^{-1}$ ) and contributes to less than 20% of the stress above 10  $ms^{-1}$ . Figure 9b 474 shows the same diagnostics but for the WBF run sampled along the track of RHB. 475 It shows that the WBF overall exhibits a similar fractional contribution to stress. 476





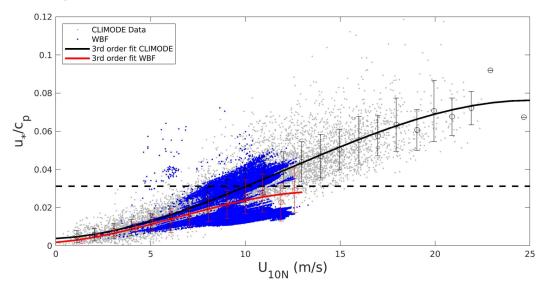


Figure 10. (a) Scatter plot of inverse peak wave age  $(u_*/c_p)$  vs.  $U_{10N}$   $(ms^{-1})$  for CLIMODE data (gray) and RHB data (a, blue). Bin-averages with the 1 standard deviation error bars are overlaid, at 1  $ms^{-1}$  interval, along with the 3rd order fit (line) for CLIMODE (black) and RHB (red). The horizontal dashed line is  $u_*/c_p = 0.03$ , denoting the threshold for fully developed seas (equivalent to  $c_p/U_{10N} = 1.2$ ). (b) As in (a) but RHB data is replaced with WBF on January 8, 2020 at 0600 UTC.

When the model is compared to the observations at this particular track and these time periods, WBF appears to accurately characterize the observed stress relationship with wave age (See also Figure 8). However, if sampled over a broader region under a specific synoptic condition featuring strong swell and moderate winds, a quite different result is obtained. Figure 9c shows the same results as Figure 9b, except that the entire model domain is sampled under the same synoptic condition examined in Section 3. In this case, the parameterized stress under moderately

strong 8-12  $ms^{-1}$  wind speeds supported by Regime 2 (orange) is comparable to the 484 stress supported by Regime 1 (blue). This is different from the result from Figure 485 9b but is consistent with the significantly reduced stress over wave age of 1.7-3 and 486 wind speeds of 8-12  $ms^{-1}$  shown in Figure 6. This indicates that, because the RHB sampled mainly in the Tradewind Alley region, it did not capture other regions un-488 der the same synoptic condition where WBF assumes that the swell corresponding 489 to the spectral peak support the lower wind stress despite the moderately strong 490 wind speeds of 8-12  $ms^{-1}$ . Since, in reality, short wind-waves under such wind 491 speeds should still support the increased stress despite the higher wave age, we be-492 lieve this is a form of deficiency in COARE3.5 WBF in representing the wind stress 493 over mixed swell-dominated seas.

In fact, the COARE3.5's WBF was developed and tuned primarily by using 495 the wave data collected from the extratropics, where sea state tends to be dominated 496 by growing and fully-developed waves under high winds (see Figure 2 in Edson et 497 al., 2013). Figure 10 compares the sea state used to tune COARE3.5, taken during 100 the CLIMODE campaign (CLIVAR Mode Water Dynamic Experiment, Marshall et al., 2009), with the sea state observed by RHB during January-February 2020 and 500 modeled in WBF on January 8, 2020 at 0600 UTC in the ATOMIC region. It shows 501 the relationship between the inverse wave age and  $U_{10N}$ . Here, a low inverse wave 502 age is indicative of decaying seas and swells. An inverse wave age of 0.03 (dashed 503 line) is roughly equivalent to an equilibrium wave age of 1.2. As expected, the sea 504 state captured in the ATOMIC region is very different and much older than the 505 one used in COARE3.5. Therefore the wind stress under moderate winds and swell 506 dominated conditions observed here, and possibly in other tropical oceans, may not be currently well parameterized in the COARE3.5 WBF. The specific deficiency 508 identified from this analysis is that, for mixed seas (Regime 2) where high wave age 509 and moderately strong wind co-occur, the current COARE3.5 WBF overemphasizes 510 the swell impact on wind stress, leading to the low-stress bias despite the moderately 511 strong winds. 512

#### 513 5 The revised wave-based formulation in COARE3.5

In the following, we present two experimental revisions to the  $z_0$  formulation in 514 the current COARE3.5 WBF for swell conditions coincident with moderate to high 515 winds, the condition that is frequently observed in the northern ATOMIC region 516 in the boreal winter. One method is to replace the peak wave period  $(T_p)$  with the 517 mean wave period  $(T_m)$  in the definition of the phase speed and thus wave age, and 518 another is to incorporate the effect of misaligned waves with local wind on aerody-519 namic roughness in the  $z_0$  parameterization. In essence, these two observationally-520 guided approaches desensitize the impact of swell on  $z_0$  and  $\tau$  estimates at moderate 521 winds and alleviate the low biases in the current COARE3.5 WBF. For this, we now 522 return to the case study on January 8, 2020 as in Section 3. 523

# 5.1 The mean wave period

One possible approach to mitigate the overestimation of the swell impact on 525  $z_0$  and  $\tau$  under moderate to high winds is to use the wave's mean period,  $T_m$ , to 526 calculate the average phase speed,  $c_m$ , in the wave age definition. This change is mo-527 tivated by the finding that  $T_p$  does not accurately describe a mixed-sea state where 528 swell and wind-sea co-exist, as shown in Figure 10.  $T_p$  can be also sensitive to the 529 spectral shape of the wave energy and the chosen filter, while  $T_m$  can be reliably es-530 timated from observations and WW3 as either an energy-weighted average period or 531 zero-crossing period. A similar argument has been made recently by (Colosi et al., 532

<sup>524</sup> 

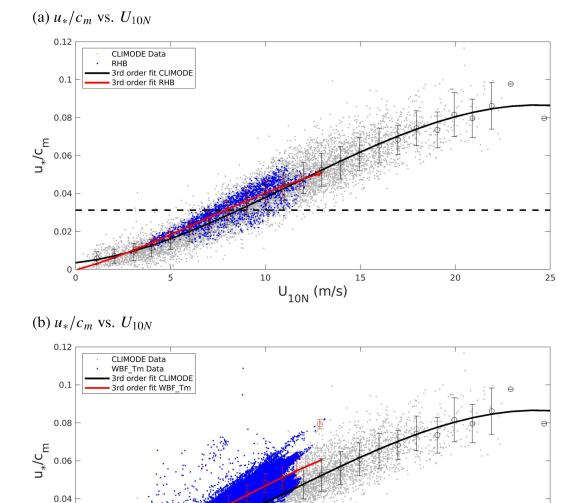


Figure 11. (a) As in Figure 10a but with inverse mean wave age  $(u_*/c_m)$ . The dashed line is  $u_*/c_m = 0.03$ , denoting the threshold for fully developed seas (equivalent to  $c_m/U_{10N} = 1.2$ ). (b) As in Figure 10b except for showing the result from WBF<sub>-</sub> $T_m$ 

U<sub>10N</sub> (m/s)

15

<sup>533</sup> 2021) as they chose to use a wave age dependent computed with the mean period to
 <sup>534</sup> construct the seasonal probability of swell over global oceans.

10

0.02

0

0

<sup>535</sup> We carried out an additional coupled simulation, dubbed WBF\_ $T_m$ , where  $T_p$ <sup>536</sup> is replaced with  $T_m$  to get the mean phase speed of the waves  $c_m$  in Eq. 12:

$$z_{rough} = H_s D(\frac{u_*}{c_m})^B,\tag{12}$$

20

25

where D=0.39 and B=2.6, which have been tuned using the COARE3.5 set of observations. We will estimate  $T_m$  based on the zero-crossing period as it is the

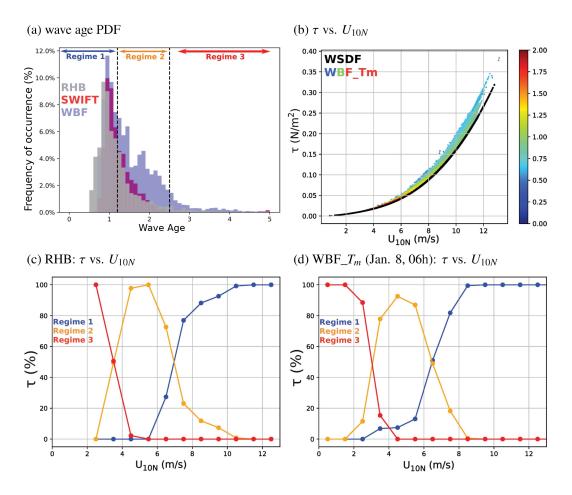


Figure 12. (a) Mean wave age distributions estimated from RHB (gray), SWIFT (red), and WBF\_ $T_m$  (blue). WBF\_ $T_m$  is sampled along-track of the RHB and SWIFT. (b) Scatter plot of  $\tau$  (Nm<sup>-2</sup>) vs.  $U_{10N}$  ( $ms^{-1}$ ) from WSDF in black and WBF\_ $T_m$  color-coded to denote the corresponding wave age on January 8, 2020 at 0600 UTC. (c,d) As in Figure 9a,c, except that the wave age is defined with  $T_m$  for (c) RHB and (d) WBF\_ $T_m$ .

one used to describe  $T_m$  in the observation. Figure 11 shows the same diagnostics 539 as in Figure 10 but this time using  $c_m$  to calculate the inverse wave age in both the 540 observations, CLIMODE and RHB, and the WBF  $T_m$  run. The general trend of 541 both sets of observations are now in good agreement (Fig. 11a). In WBF  $T_m$ , the 542 use of  $c_m$  in eq. 12 alleviates the bias over the mixed sea (Regime 2) (Figure 10b vs. 543 Fig. 11b) and shows a better agreement of the general trends from the observations. 544 Further refinement of coefficients in eq. 12 will be addressed in more detail in the 545 future release of the COARE4.0 algorithm. 546

Figure 12a shows the PDF of wave age for RHB (gray), SWIFT (red), and 547 WBF  $T_m$  (blue) computed using  $T_m$ . This figure should be compared to Figure 8a 548 where RHB, SWIFT and WBF wave age PDFs were computed using  $T_p$ . Similar to 549 Figure 8a, wave age is capped at 5 to show the tail of the distribution. In contrast 550 to the bi-modal distribution of wave age with the pronounced secondary peak of 551 wave age estimate with  $T_p$ , the use of  $T_m$  effectively removes this secondary peak 552 in both the model and observations, yielding a markedly different distribution with 553 an overall prevalence of younger sea state. We adjusted the different categories of 554 wave age defined previously to fit the new wave age distribution based on  $T_m$ . Fig-555

ure 12b shows  $\tau$  on January 8, 2020 at 0600 UTC from WBF- $T_m$ , with wave age 556 color-coded. The cluster of low  $z_0$  with high wave age seen in Figure 4b is elimi-557 nated in WBF  $T_m$ , because of the elevated  $z_0$  and  $\tau$  under moderate to high wind 558 speeds. Finally, Figure 12c,d, to be compared to Figure 9a,c shows the percentage of 559  $\tau$  supported by each category of wave age for RHB and for WBF<sub>T</sub>, respectively. 560 With the use of  $T_m$ , WBF<sub>-</sub> $T_m$  agrees well with RHB concerning the fractional con-561 tribution from each sea state to the surface stress. Particularly over 7  $ms^{-1}$ , most of 562 the contribution to  $\tau$  now comes from the wind sea (blue), whereas the contribution 563 of mature seas and swell subsides rapidly with the increased wind speeds. This is 564 a clear improvement from  $\tau$  parameterized using  $T_p$  (Figure 9c) and is much more 565 consistent with the observations (Figures 9a, 12c). 566

#### 567

#### 5.2 Including the (mis)aligned wind-wave directions

As discussed in Section 2, the COARE3.5 assumes the wave stress as a scalar 568 roughness parameter, and hence the direction of wave-stress vectors is aligned with 569 the mean wind vectors. However, wave stress and mean wind vectors can be mis-570 aligned under various conditions, including under rapidly translating storms (e.g., 571 S. S. Chen et al., 2013), near strong vorticity and divergence gradients and density 572 fronts (e.g., Villas Bôas & Young, 2020), or over mixed seas where wind waves and 573 swells co-exist under high winds. Such nonequilibrium wave motions can influence 574 wave slope, roughness length, and wind stress (Janssen, 1991; Rieder et al., 1994; 575 Zou et al., 2019; Patton et al., 2019; Porchetta et al., 2021; Deskos et al., 2021). 576 Here, we attempt to incorporate the directionality of the wind and waves following 577

Patton et al. (2019) and Porchetta et al. (2019), such that

$$z_{rough} = H_s Dcos(a\theta) (\frac{u_*}{c_p})^{Bcos(b\theta)}.$$
(13)

D and B are the coefficients taken from COARE3.5 (See Eq. 8), while the 579 coefficients a = 0.4 and b = 0.32 are adopted from (Porchetta et al., 2019). In prin-580 ciple, all these coefficients require site-specific tunings. For example, (Porchetta et 581 al., 2019) used the high wind conditions observed from the FINO platform in the 582 North Sea and the Air-Sea Interaction Tower (ASIT) in the New England Shelf, 583 which represents different wind speed and wave age conditions from the trade-wind 584 and swell-dominated tropical oceans as in the ATOMIC domain. Additional tun-585 ing exploiting direct momentum flux measurements would be needed to develop a 586 refined set of coefficients for the tropical oceans. This is beyond the scope of the 587 study. Using this new formulation, we conducted an additional coupled experiment, 588 dubbed  $WBF_{-\theta}$ , which is to be compared to the default wave-based formulation in 589 COARE3.5, where  $\theta = 0$ . 590

Figure 13a compares the parameterized  $\tau$ , color-coded by the angle ( $\theta$ ) be-591 tween the wind direction and peak wave direction in WBF. It shows that the lower 592  $\tau$  from WBF compared to WSDF (and also observations) occurs when the swell 593 waves are strongly misaligned with winds (e.g.,  $\theta > 60-90^{\circ}$ ). This indicates that 594 the assumption of  $\theta = 0$  in WBF can be attributed to the lower  $\tau$ . When the di-595 rectional misalignments are considered in the roughness length parameterization in 596 COARE3.5 (Figure 13b),  $\tau$  over the misaligned waves has been effectively elevated 597 as the waves opposing the wind increase the surface drag. This is shown to reduce 598 the low  $\tau$  bias significantly. 599

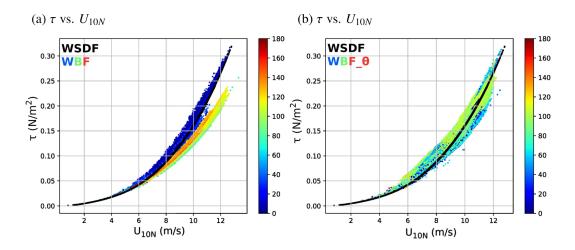


**Figure 13.** (a) Scatter plot of parameterized  $\tau$  (Nm<sup>-2</sup>) vs.  $U_{10N}$  ( $ms^{-1}$ ) from WSDF in black and WBF color-coded to denote the corresponding wind-wave angle ( $\theta$ ) on January 8, 2020 at 0600UTC. Note that in the  $z_0$  formulation in WBF assumes  $\theta = 0$ . (b) As in (a) except from WBF\_ $\theta$ , where  $\theta$  is treated as a non-zero quantity in the  $z_0$  formulation.

# 600 6 Conclusion

This study investigated the role of surface waves in surface roughness length 601  $(z_0)$  and surface stress  $(\tau)$  in the persistent and strong trade winds and swell-602 dominated Northwestern Atlantic Ocean during the boreal winter season. The main 603 objective is to evaluate how accurately the air-sea momentum flux is represented 604 in advanced bulk flux algorithms such as COARE3.5 when compared to the direct 605 surface flux measurements. The study then identifies the wind speed and wave age 606 regimes where the wave-based formulation (WBF) in the COARE3.5 exhibits de-607 ficiencies, and explores possible approaches to mitigating the deficiencies. In this 608 investigation, estimated  $z_0$  and  $\tau$  from four different SCOAR ocean-atmosphere-wave 609 coupled model simulations are compared to each other and with direct observa-610 tions over the range of observed wind speeds and wave ages. These experiments are 611 identical except for the  $z_0$  formulation in COARE3.5. 612

To facilitate the unambiguous identification of the immediate impacts of dif-613 ferent  $z_0$  formulations without contribution from the feedback effects which affect 614 the state variables, the two short simulations from WSDF and WBF are compared 615 first. The results show that the estimated  $z_0$  and  $\tau$  differences strongly depend on 616 wind speeds and wave age regimes. In the case of wind sea or fully-developed sea, 617 the incorporation of the wave impacts via wave age and wave slope increases  $z_0$ 618 (Figure 4d) and  $\tau$  (Figure 6b). The increase is expected, since the young seas under 619 high winds are characterized by the enhanced wave slope and choppy surface (Figure 620 5b), which effectively increases the surface drag, and  $\tau$ . The increased surface drag 621 decelerates the near-surface winds (Figure 6c), consistent with the positive change in 622 wind work due to the inclusion of waves (Figure 6d). 623

However, in the mixed sea condition, where moderate to high wind speeds (10 to 12  $ms^{-1}$ ) co-occur with decaying swell, the WBF tends to underestimate  $z_0$  compared to the WSDF and  $\tau$  compared to the measurements. The weak stress then accelerates the near-surface wind speed by 5% over the region of negative change in wind work (Figure 6d). The sea state in this high wave age is characterized by an aerodynamically smooth sea surface with a low wave slope (Figure 5b) and strongly misaligned waves with local winds (Figure 5d), indicating the presence of remotelygenerated swell. However, despite the swell-dominated sea state, the observations suggest that the wind seas in this mixed sea condition should continue to support the momentum flux due to moderate-to-high wind speeds, thereby increasing  $\tau$  with wind speed (Figure 7). The current COARE3.5 WBF, on the other hand, overemphasizes the role of swell on  $z_0$  and predicts a decreased  $\tau$  under moderate wind conditions.

The different approaches were explored in this study to alleviate the low-stress 637 bias in the COARE3.5 WBF under the mixed sea regime. The first approach in-638 volves re-defining wave age using the mean period of the waves to better represent 639 the wave period in the mixed sea condition (Figure 4a). The second approach takes 640 advantage of the fully coupled model by considering the directionality of waves with 641 respect to winds (Eq. 12), the vital missing process in the current COARE3.5 WBF 642 and many numerical modeling studies except for a limited number of Large Eddy 643 Simulations (LES) and offshore wind energy studies (See Review by Patton et al., 644 2019). Our results show that both approaches produce equivalent results by effec-645 tively boosting  $z_0$  and  $\tau$  under the misaligned waves under moderate-to-high winds. 646

Our analysis reveals a notable deficiency in the ocean-wave and wave-647 atmosphere coupling components of the coupled model, which guides the direction 648 of our future investigation. That is, the frequency of swell simulated by the coupled 649 WW3 model is overestimated compared to the in situ observations (Figure 8a), more 650 so with the use of peak wave period but nonetheless noticeable with the use of mean 651 period. Since the wave model provide the parameters required by the WBF, some 652 of the issues described above are a result of inaccurate inputs as well as problems 653 with the parameterization. The tendency toward the higher wave age indicates that 654 the model under-represents critical dissipation mechanisms of the swell energy, and 655 waves in general, which likely have contributed to the low-stress bias. There are at 656 least two possible factors to consider. 657

First, the primary loss of swell energy is to the atmosphere in situations where 658 the swell waves outrun the winds or propagate in the opposite direction to the lo-659 cal wind (e.g., Donelan, 1999; Rascle et al., 2008; Kahma et al., 2016; Liu et al., 660 2017). Tropical oceans, including our study region, have many low-wind regimes, 661 where the wave-driven low-level wind jet (Harris, 1966) and turbulent mixing in the MABL (Kantha, 2006; Ardhuin & Jenkins, 2006; Babanin, 2006) constitute impor-663 tant sources for attenuation of the swell energy (Ardhuin et al., 2009; S. Chen et al., 664 2019). It is quite possible that the processes related to the upward flux of momen-665 tum and energy over swell are not adequately captured in our coupled wind-wave 666 model. Previous studies find that the wave-driven wind jet is at heights of 5-10 m 667 (Sullivan et al., 2008; Smedman et al., 2009). However, our experiments used the 668 default vertical grid system in WRF, where the wind at the lowest height of the 669 model is typically 30–50 m. The WRF PBL scheme expects this level to be within 670 the constant-flux layer, where similarity theory is applied (Aligo et al., 2009; Shin 671 et al., 2012). Yet, this level can be above the surface layer, especially in the low-672 wind and stable boundary layer conditions, as often observed in the northern part 673 of the ATOMIC domain. If the turbulent mixing between the lowest model level 674 and the swell at the sea surface is weak, the upward energy and momentum fluxes 675 from the swell to the wind are likely to be under-represented. This might have been 676 exacerbated by using a local PBL scheme (MYNN) in our model. 677

Moreover, parameterizations for the so-called negative wind input exist in standalone WW3 model through the use of the source term packages of wind input (Donelan et al., 2006; Ardhuin et al., 2010; Babanin, 2011; Rogers et al., 2012; Liu et al., 2017, 2019). With this, the standalone WW3 model forced with winds should better capture the loss of energy of swell waves. Yet, it is unclear how such parameterizations should be incorporated into the coupled model, as they do not represent

the actual gain of momentum by the wind from the swell. Our future work will focus

- on adequately representing the near-surface wind responses to swell waves in the
- atmospheric model.

Secondly, the wave breaking and the induced near-surface mixing would in-687 fluence the wave energy growth and attenuation (e.g., Kudryavtsev et al., 2014). 688 Also, Iyer et al. (2022), using the SWIFT drifters deployed during the ATOMIC 689 campaign, showed that wave-current interactions can generate significant spatial 690 and temporal variability in momentum fluxes in this region. However here, since the 691 current study does not include wave-ocean coupling, the question about the impacts 692 of ocean-wave coupling on the skill of the simulated wave fields cannot be addressed. 693 This is a subject of ongoing efforts. 694

# <sup>695</sup> 7 Open Research

The observational datasets from the ATOMIC and EUREC<sup>4</sup>A experiments are 696 available from https://observations.ipsl.fr/aeris/eurec4a/#/. ERA5 At-697 mospheric hourly reanalyses were made available by the Copernicus Climate Change 698 Service (Hersbach et al., 2018a, 2018b); Mercator Ocean International daily analyses 699 were made available by the Copernicus Marine Environment Monitoring Service: 700 (dataset: https://doi.org/10.48670/moi-00016, last access: 31 January 2022); 701 global 3-hourly spectral wave analyses were made available by Ifremer (dataset: 702 ftp://ftp.ifremer.fr/ifremer/ww3/HINDCAST/GLOBAL, last access: 31 January 703 2022); SO-HYBAM (Amazon Basin Water Resources Observation Service) data are 704 freely available upon registration at https://hybam.obs-mip.fr. 705

WaveWatchIII model is distributed using GitHub (https://github.com/
NOAA-EMC/WW3, last access: 31 January 2022). WRF model is distributed using
GitHub (https://github.com/wrf-model/WRF, last access: 31 January 2022).
ROMS model is freely available upon registration at https://www.myroms.org/.
The SCOAR code is available through the GitHub repository: https://github
.com/hyodae-seo/SCOAR.

#### 712 Acknowledgments

<sup>713</sup> This research was supported by NOAA (NA19OAR4310376), NASA

(80NSSC21K1524), and NSF (OCE-2148120). HS also acknowledges the additional

<sup>715</sup> support from NSF (OCE-2022846) and NOAA (NA17OAR4310255). The computing

resources were provided by the WHOI High-Performance Computing Facility. The

authors thank the ATOMIC and EUREC<sup>4</sup>A team for providing the observational

datasets (https://observations.ipsl.fr/aeris/eurec4a/#/). The authors also thank

<sup>719</sup> Elizabeth Thompson, Jim Thomson, Suneil Iyer, Ludovic Bariteau, Kyla Drushka,

<sup>720</sup> Chris Fairall and Denis Bourras for their insightful comments.

# 721 **References**

- Aligo, E. A., Gallus, W. A., & Segal, M. (2009). On the impact of WRF model ver tical grid resolution on Midwest summer rainfall forecasts. Wea. Forecasting,
   24, 575–594.
- Ardhuin, F., Chapron, B., & Collard, F. (2009). Observation of swell dissipation
   across oceans. *Geophys. Res. Lett.*, 36(6). doi: 10.1029/2008GL037030
- Ardhuin, F., & Jenkins, A. D. (2006). On the Interaction of Surface Waves and
   Upper Ocean Turbulence. Journal of Physical Oceanography, 36(3), 551 557.
   doi: 10.1175/JPO2862.1
- <sup>730</sup> Ardhuin, F., O'Reilly, W. C., Herbers, T. H. C., & Jessen, P. F. (2003). Swell

731	Transformation across the Continental Shelf. Part I: Attenuation and
732	Directional Broadening. J. Phys. Oceanogr., 33(9), 1921-1939. doi:
733	10.1175/1520-0485(2003)033(1921:STATCS)2.0.CO;2
734	Ardhuin, F., Rogers, E., Babanin, A. V., Filipot, JF., Magne, R., Roland, A.,
735	Collard, F. (2010). Semiempirical Dissipation Source Functions for Ocean
736	Waves. Part I: Definition, Calibration, and Validation. J. Phys. Oceanogr.,
737	40(9), 1917-1941. doi: 10.1175/2010JPO4324.1
738	Ardhuin, F., & Roland, A. (2012). Coastal wave reflection, directional spread,
739	and seismoacoustic noise sources. J. Geophys. Res., $117(C11)$ . doi:
740	10.1029/2011JC007832
741	Babanin, A. V. (2006). On a wave-induced turbulence and a wave-mixed upper
742	ocean layer. Geophysical Research Letters, 33(20). doi: https://doi.org/10
743	.1029/2006GL027308
744	Babanin, A. V. (2011). Breaking and Dissipation of Ocean Surface Waves. Cam-
745	bridge University Press. doi: 10.1017/CBO9780511736162
746	Battjes, J., & Janssen, J. (1978, Jan.). Energy loss and set-up due to breaking of
747	random waves. Coastal Engineering Proceedings, 1, 32. doi: 10.9753/icce.v16
748	
749	Bourras, D., Branger, H., Luneau, C., Reverdin, G., Speich, S., Geykens, N.,
750	Clémençon, A. (2020). EUREC4A-OA_OCARINA : OCARINA
751	Air-Sea Flux Data. SEANOE. (Accessed 23 December 2021) doi: https://doi.org/10.17882/77479
752	- ,, ., ,
753	Bourras, D., Geyskens, N., Reverdin, G., Clémençon, A., Barrois, H., Branger, H., & Luneau, C. (2020). EUREC4A-OA experiment: Air-Sea Flux Mast Data. SEA-
754	NOE. (Accessed 23 December 2021) doi: https://doi.org/10.17882/77341
755	Charnock, H. (1955). Wind stress on a water surface. Quart. J. Roy. Meteor. Soc.,
756 757	81(350), 639-640. doi: 10.1002/qj.49708135027
758	Chen, F., & Dudhia, J. (2001). Coupling an Advanced Land Surface–Hydrology
759	Model with the Penn State–NCAR MM5 Modeling System. Part I: Model Im-
760	plementation and Sensitivity. Monthly Weather Review, 129(4), 569 - 585. doi:
761	10.1175/1520-0493(2001)129(0569:CAALSH>2.0.CO;2
762	Chen, S., Qiao, F., Jiang, W., Guo, J., & Dai, D. (2019). Impact of Surface Waves
763	on Wind Stress under Low to Moderate Wind Conditions. Journal of Physical
764	Oceanography, 49(8), 2017 - 2028. doi: 10.1175/JPO-D-18-0266.1
765	Chen, S. S., Zhao, W., Donelan, M. A., & Tolman, H. L. (2013). Directional
766	wind–wave coupling in fully coupled atmosphere–wave–ocean models: Re-
767	sults from cblast-hurricane. Journal of the Atmospheric Sciences, $70(10)$ , 3198
768	- 3215. doi: 10.1175/JAS-D-12-0157.1
769	Chou, MD., & Suarez, M. J. (1999). A Solar Radiation Parameterization for Atmo-
770	spheric Studies. Technical Report Series on Global Modeling and Data Assimi-
771	lation, 15.
772	Colosi, L. V., Villas Bôas, A. B., & Gille, S. T. (2021). The seasonal cy-
773	cle of significant wave height in the ocean: Local versus remote forcing.
774	Journal of Geophysical Research: Oceans, 126(8), e2021JC017198. doi:
775	https://doi.org/10.1029/2021JC017198
776	Csanady, G. T., & Gibson, M. (2001). Air-Sea Interaction: Laws and Mechanisms.
777	Cambridge University Press. doi: 10.1017/CBO9781139164672
778	Deskos, G., Lee, J. C. Y., Draxl, C., & Sprague, M. A. (2021). "review of wind-wave
779	coupling models for large-eddy simulation of the marine atmospheric bound-
780	ary layer". Journal of the Atmospheric Sciences, 78(10), 3025 - 3045. doi: 10.1175/JAS-D-21-0003.1
781	Donelan, M. A. (1999). Wind-induced growth and attenuation of laboratory waves.
782 783	In: Institute of Mathematics and Its Applications Conference Series, 69, Ox-
783	ford;Clarendon, 183-194.
785	Donelan, M. A., Babanin, A. V., Young, I. R., & Banner, M. L. (2006). Wave-

786	Follower Field Measurements of the Wind-Input Spectral Function. Part II:
787	Parameterization of the Wind Input. Journal of Physical Oceanography, 36(8), 1672 - 1689. doi: 10.1175/JPO2933.1
788	Drennan, W. M., Graber, H. C., Hauser, D., & Quentin, C. (2003). On the wave
789	age dependence of wind stress over pure wind seas. Journal of Geophysical Re-
790	search: Oceans, 108(C3). doi: https://doi.org/10.1029/2000JC000715
791	Edson, J. B., Jampana, V., Weller, R., Bigorre, S., Plueddemann, A., Fairall,
792	C., Hersbach, H. (2013). On the exchange of momentum over the
793	open ocean. Journal of Physical Oceanography, 43(8), 1589 - 1610. doi:
794	10.1175/JPO-D-12-0173.1
795	Edson, J. B., Jampana, V., Weller, R. A., Bigorre, S. P., Plueddemann, A. J.,
796	Fairall, C. W., Hersbach, H. (2014). Corrigendum. Journal of
797	Physical Oceanography, 44(9), 2590 - 2590. Retrieved from https://
798	journals.ametsoc.org/view/journals/phoc/44/9/jpo-d-14-0140.1.xml
799	doi: 10.1175/JPO-D-14-0140.1
800	Egbert, G. D., & Erofeeva, S. Y. (2002). Efficient inverse modeling of barotropic
801	ocean tides. Journal of Atmospheric and Oceanic Technology, 19(2), 183 - 204.
802	doi: 10.1175/1520-0426(2002)019(0183:EIMOBO)2.0.CO;2
803	Fairall, C. W., Bradley, E. F., Hare, J. E., Grachev, A. A., & Edson, J. B. (2003).
804 805	Bulk parameterization of air-sea fluxes : Updates and verification for the
806	COARE algorithm. Journal of Climate, 16, 571-591.
807	Fairall, C. W., Bradley, E. F., Rogers, D. P., Edson, J. B., & Young, G. S. (1996).
808	Bulk parameterization of air-sea fluxes for tropical ocean-global atmosphere
809	coupled-ocean atmosphere response experiment. Journal of Geophysical Re-
810	search: Oceans, 101(C2), 3747-3764. doi: https://doi.org/10.1029/95JC03205
811	Hanley, K. E., & Belcher, S. E. (2008). Wave-Driven Wind Jets in the Marine At-
812	mospheric Boundary Layer. Journal of the Atmospheric Sciences, 65(8), 2646 -
813	2660. doi: 10.1175/2007JAS2562.1
814	Harris, D. L. (1966). The Wave-Driven Wind. Journal of Atmospheric Sciences,
815	23(6), 688 - 693. doi: $10.1175/1520-0469(1966)023(0688:TWDW)2.0.CO;2$
816	Hasselmann, S., Hasselmann, K., Allender, J. H., & Barnett, T. P. (1985). Compu-
817	tations and Parameterizations of the Nonlinear Energy Transfer in a Gravity-
818	Wave Specturm. Part II: Parameterizations of the Nonlinear Energy Transfer
819	for Application in Wave Models. J. Phys. Oceanogr., 15(11), 1378-1391. doi:
820	10.1175/1520-0485(1985)015(1378:CAPOTN)2.0.CO;2
821	Hersbach, H., Bell, B., Berrisford, P., Biavati, G., Horányi, A., Muñoz Sabater,
822	J., Thépaut, JN. (2018a). ERA5 hourly data on pressure lev-
823	els from 1979 to present. Copernicus Climate Change Service (C3S) Cli-
824	mate Data Store (CDS). Dataset. (Accessed 01 January 2022) doi:
825	https://doi.org/10.24381/cds.bd0915c6
826	Hersbach, H., Bell, B., Berrisford, P., Biavati, G., Horányi, A., Muñoz Sabater, J.,
827	Thépaut, JN. (2018b). ERA5 hourly data on single levels from 1979
828	to present. Copernicus Climate Change Service (C3S) Climate Data Store
829	(CDS). Dataset. (Accessed 01 January 2022) doi: https://doi.org/10.24381/
830	cds.adbb2d47
831	Hong, SY., & Lim, JO. J. (2006). The WRF Single-Moment 6-Class Microphysics
832	Scheme (WSM6). Journal of the Korean Meteorological Society, 42, 129-151.
833	Iyer, S., Thomson, J., Thompson, E., & Drushka, K. (2022). Variations in wave
834	slope and momentum flux from wave-current interactions in the tropical trade
835	winds. Journal of Geophysical Research: Oceans, 127(3), e2021JC018003. doi: https://doi.org/10.1020/2021JC018002
836	https://doi.org/10.1029/2021JC018003
837	Iyer, S., Thomson, J., Thompson, E. J., & Drushka, K. (2021). Variations
838	in wave slope and momentum flux from wave-current interactions in the tropical trade winds. <i>Earth and Space Science Open Archive</i> , 51. doi:
839	10.1002/essoar.10508004.1
840	10.1002/050001.10000004.1

841	Janssen, P. A. E. M. (1989). Wave-induced stress and the drag of air flow over sea
842	waves. Journal of Physical Oceanography, 19(6), 745 - 754. doi: 10.1175/1520
843	-0485(1989)019(0745:WISATD)2.0.CO;2
844	Janssen, P. A. E. M. (1991). Quasi-linear theory of wind-wave generation applied to
845	wave forecasting. J. Phys. Oceanogr., $21(11)$ , 1631-1642.
846	Jiang, H., & Chen, G. (2013). A Global View on the Swell and Wind Sea Climate
847	by the Jason-1 Mission: A Revisit. Journal of Atmospheric and Oceanic Tech-
848	nology, 30(8), 1833 - 1841. doi: $10.1175/JTECH-D-12-00180.1$
849	Jiménez, P. A., Dudhia, J., González-Rouco, J. F., Navarro, J., Montávez, J. P.,
850	& García-Bustamante, E. (2012). A Revised Scheme for the WRF Sur-
851	face Layer Formulation. Monthly Weather Review, $140(3)$ , 898 - 918. doi:
852	10.1175/MWR-D-11-00056.1
853	Kahma, K. K., Donelan, M. A., Drennan, W. M., & Terray, E. A. (2016). Evi-
854	dence of Energy and Momentum Flux from Swell to Wind. Journal of Physical
855	<i>Oceanography</i> , 46(7), 2143 - 2156. doi: 10.1175/JPO-D-15-0213.1
856	Kantha, L. (2006). A note on the decay rate of swell. Ocean Modelling, 11(1), 167-
857	173. doi: https://doi.org/10.1016/j.ocemod.2004.12.003
858	Kudryavtsev, V., Chapron, B., & Makin, V. (2014). Impact of wind waves on the
859	air-sea fluxes: A coupled model. Journal of Geophysical Research: Oceans,
860	119(2), 1217-1236. doi: https://doi.org/10.1002/2013JC009412
861	Large, W. G., McWilliams, J. C., & Doney, S. C. (1994). Oceanic vertical mixing: A review and a model with a nonlocal boundary layer parameterization. <i>Reviews</i>
862	of Geophysics, 32(4), 363-403. doi: https://doi.org/10.1029/94RG01872
863	Lellouche, JM., Greiner, E., Le Galloudec, O., Garric, G., Regnier, C., Drevillon,
864 865	M., Le Traon, PY. (2018). Recent updates to the Copernicus Marine
866	Service global ocean monitoring and forecasting real-time $1/12^{\circ}$ high-resolution
867	system. Ocean Science, $14(5)$ , 1093–1126. doi: 10.5194/os-14-1093-2018
868	Liu, Q., Babanin, A., Fan, Y., Zieger, S., Guan, C., & Moon, IJ. (2017). Nu-
869	merical simulations of ocean surface waves under hurricane conditions: As-
870	sessment of existing model performance. Ocean Modelling, 118, 73-93. doi:
871	https://doi.org/10.1016/j.ocemod.2017.08.005
872	Liu, Q., Rogers, W. E., Babanin, A. V., Young, I. R., Romero, L., Zieger, S.,
873	Guan, C. (2019). Observation-based source terms in the third-generation wave
874	model wavewatch iii: Updates and verification. Journal of Physical Oceanogra-
875	phy, 49(2), 489 - 517. doi: 10.1175/JPO-D-18-0137.1
876	Marshall, J., Ferrari, R., Forget, G., Maze, G., Andersson, A., Bates, N.,
877	Thomas, L. (2009). The Climode Field Campaign: Observing the Cy-
878	cle of Convection and Restratification over the Gulf Stream. Bulletin of
879	the American Meteorological Society, $90(9)$ , 1337 - 1350. doi: 10.1175/
880	2009BAMS2706.1
881	Moon, IJ., Hara, T., Ginis, I., Belcher, S. E., & Tolman, H. L. (2004). Effect of
882	surface waves on air-sea momentum exchange. part i: Effect of mature and
883	growing seas. Journal of the Atmospheric Sciences, 61(19), 2321 - 2333. doi:
884	10.1175/1520-0469(2004)061(2321:EOSWOA)2.0.CO;2
885	Nakanishi, M., & Niino, H. (2004). An Improved Mellor–Yamada Level-3 Model
886	with Condensation Physics: Its Design and Verification. Boundary-Layer Mete-
887	orology, 112, 1-31. doi: 10.1023/B:BOUN.0000020164.04146.98
888	Nakanishi, M., & Niino, H. (2006). An Improved Mellor–Yamada Level-3 Madeli Ita Numerical Stability and Application to a Paricanal Predia
889	Model: Its Numerical Stability and Application to a Regional Predic- tion of Advection Fog. Boundary-Layer Meteorology, 119, 397-407. doi:
890	tion of Advection Fog. Boundary-Layer Meteorology, 119, 397-407. doi: 10.1007/s10546-005-9030-8
891	Nakanishi, M., & Niino, H. (2009). Development of an improved turbulence closure
892	model for the atmospheric boundary layer. Journal of the Meteorological Soci-
893 894	ety of Japan. Ser. II, 87(5), 895-912. doi: 10.2151/jmsj.87.895
334	
895	Oost, W., Komen, G., Jacobs, C., & Van Oort, C. (2002). New evidence for a

896	relation between wind stress and wave age from measurements during AS-
897	GAMAGE. Boundary-Layer Meteorology volume, 103(3), 409 - 438. doi: 10.1023/A:1014913624535
898	Patton, E. G., Sullivan, P. P., Kosović, B., Dudhia, J., Mahrt, L., Žagar, M., &
899	Marić, T. (2019). On the influence of swell propagation angle on surface drag.
900	Journal of Applied Meteorology and Climatology, 58(5), 1039 - 1059. doi:
901 902	10.1175/JAMC-D-18-0211.1
903	Phillips, O. M. (1985). Spectral and statistical properties of the equilibrium range in
904 905	wind-generated gravity waves. Journal of Fluid Mechanics, 156, 505–531. doi: 10.1017/S0022112085002221
906	Porchetta, S., Temel, O., Muñoz Esparza, D., Reuder, J., Monbaliu, J., van Beeck,
907	J., & van Lipzig, N. (2019). A new roughness length parameterization ac-
908	counting for wind-wave (mis)alignment. Atmospheric Chemistry and Physics,
909	19(10), 6681–6700. doi: 10.5194/acp-19-6681-2019
910	Porchetta, S., Temel, O., Warner, J., Muñoz-Esparza, D., Monbaliu, J., van Beeck,
911	J., & van Lipzig, N. (2021). Evaluation of a roughness length parametrization
912	accounting for wind–wave alignment in a coupled atmosphere–wave model.
913	Quarterly Journal of the Royal Meteorological Society, 147(735), 825-846. doi:
914	https://doi.org/10.1002/qj.3948
915	Quinn, P. K., Thompson, E. J., Coffman, D. J., Baidar, S., Bariteau, L., Bates,
916	T. S., Zuidema, P. (2021). Measurements from the RV Ronald H. Brown
917	and related platforms as part of the Atlantic Tradewind Ocean-Atmosphere
918	Mesoscale Interaction Campaign (ATOMIC). Earth System Science Data,
919	13(4), 1759-1790. doi: $10.5194/essd-13-1759-2021$
920	Rascle, N., & Ardhuin, F. (2013). A global wave parameter database for geophysical
921	applications. Part 2: Model validation with improved source term parame-
922	terization. Ocean Modelling, 70, 174 - 188. (Ocean Surface Waves) doi:
923	10.1016/j.ocemod.2012.12.001
924	Rascle, N., Ardhuin, F., Queffeulou, P., & Croizé-Fillon, D. (2008). A global
	Rascle, N., Ardhuin, F., Queffeulou, P., & Croizé-Fillon, D. (2008). A global wave parameter database for geophysical applications. part 1: Wave-
924	Rascle, N., Ardhuin, F., Queffeulou, P., & Croizé-Fillon, D. (2008). A global wave parameter database for geophysical applications. part 1: Wave- current-turbulence interaction parameters for the open ocean based on
924 925	Rascle, N., Ardhuin, F., Queffeulou, P., & Croizé-Fillon, D. (2008). A global wave parameter database for geophysical applications. part 1: Wave- current-turbulence interaction parameters for the open ocean based on traditional parameterizations. <i>Ocean Modelling</i> , 25(3), 154-171. doi:
924 925 926 927 928	Rascle, N., Ardhuin, F., Queffeulou, P., & Croizé-Fillon, D. (2008). A global wave parameter database for geophysical applications. part 1: Wave- current-turbulence interaction parameters for the open ocean based on traditional parameterizations. <i>Ocean Modelling</i> , 25(3), 154-171. doi: https://doi.org/10.1016/j.ocemod.2008.07.006
924 925 926 927 928 929	<ul> <li>Rascle, N., Ardhuin, F., Queffeulou, P., &amp; Croizé-Fillon, D. (2008). A global wave parameter database for geophysical applications. part 1: Wave-current-turbulence interaction parameters for the open ocean based on traditional parameterizations. Ocean Modelling, 25(3), 154-171. doi: https://doi.org/10.1016/j.ocemod.2008.07.006</li> <li>Renault, L., McWilliams, J. C., &amp; Penven, P. (2017). Modulation of the Agulhas</li> </ul>
924 925 926 927 928 929 930	<ul> <li>Rascle, N., Ardhuin, F., Queffeulou, P., &amp; Croizé-Fillon, D. (2008). A global wave parameter database for geophysical applications. part 1: Wave-current-turbulence interaction parameters for the open ocean based on traditional parameterizations. Ocean Modelling, 25(3), 154-171. doi: https://doi.org/10.1016/j.ocemod.2008.07.006</li> <li>Renault, L., McWilliams, J. C., &amp; Penven, P. (2017). Modulation of the Agulhas Current Retroflection and Leakage by Oceanic Current Interaction with the</li> </ul>
924 925 926 927 928 929 930 931	<ul> <li>Rascle, N., Ardhuin, F., Queffeulou, P., &amp; Croizé-Fillon, D. (2008). A global wave parameter database for geophysical applications. part 1: Wave-current-turbulence interaction parameters for the open ocean based on traditional parameterizations. Ocean Modelling, 25(3), 154-171. doi: https://doi.org/10.1016/j.ocemod.2008.07.006</li> <li>Renault, L., McWilliams, J. C., &amp; Penven, P. (2017). Modulation of the Agulhas Current Retroflection and Leakage by Oceanic Current Interaction with the Atmosphere in Coupled Simulations. Journal of Physical Oceanography, 47(8),</li> </ul>
924 925 926 927 928 929 930 931 932	<ul> <li>Rascle, N., Ardhuin, F., Queffeulou, P., &amp; Croizé-Fillon, D. (2008). A global wave parameter database for geophysical applications. part 1: Wave-current-turbulence interaction parameters for the open ocean based on traditional parameterizations. Ocean Modelling, 25(3), 154-171. doi: https://doi.org/10.1016/j.ocemod.2008.07.006</li> <li>Renault, L., McWilliams, J. C., &amp; Penven, P. (2017). Modulation of the Agulhas Current Retroflection and Leakage by Oceanic Current Interaction with the Atmosphere in Coupled Simulations. Journal of Physical Oceanography, 47(8), 2077 - 2100. doi: 10.1175/JPO-D-16-0168.1</li> </ul>
924 925 926 927 928 929 930 931 932 933	<ul> <li>Rascle, N., Ardhuin, F., Queffeulou, P., &amp; Croizé-Fillon, D. (2008). A global wave parameter database for geophysical applications. part 1: Wave-current-turbulence interaction parameters for the open ocean based on traditional parameterizations. Ocean Modelling, 25(3), 154-171. doi: https://doi.org/10.1016/j.ocemod.2008.07.006</li> <li>Renault, L., McWilliams, J. C., &amp; Penven, P. (2017). Modulation of the Agulhas Current Retroflection and Leakage by Oceanic Current Interaction with the Atmosphere in Coupled Simulations. Journal of Physical Oceanography, 47(8), 2077 - 2100. doi: 10.1175/JPO-D-16-0168.1</li> <li>Renault, L., Molemaker, M. J., Gula, J., Masson, S., &amp; McWilliams, J. C. (2016).</li> </ul>
924 925 926 927 928 929 930 931 932 933 933	<ul> <li>Rascle, N., Ardhuin, F., Queffeulou, P., &amp; Croizé-Fillon, D. (2008). A global wave parameter database for geophysical applications. part 1: Wave-current-turbulence interaction parameters for the open ocean based on traditional parameterizations. Ocean Modelling, 25(3), 154-171. doi: https://doi.org/10.1016/j.ocemod.2008.07.006</li> <li>Renault, L., McWilliams, J. C., &amp; Penven, P. (2017). Modulation of the Agulhas Current Retroflection and Leakage by Oceanic Current Interaction with the Atmosphere in Coupled Simulations. Journal of Physical Oceanography, 47(8), 2077 - 2100. doi: 10.1175/JPO-D-16-0168.1</li> <li>Renault, L., Molemaker, M. J., Gula, J., Masson, S., &amp; McWilliams, J. C. (2016). Control and Stabilization of the Gulf Stream by Oceanic Current Interaction</li> </ul>
924 925 926 927 928 930 931 932 933 934 935	<ul> <li>Rascle, N., Ardhuin, F., Queffeulou, P., &amp; Croizé-Fillon, D. (2008). A global wave parameter database for geophysical applications. part 1: Wave-current-turbulence interaction parameters for the open ocean based on traditional parameterizations. Ocean Modelling, 25(3), 154-171. doi: https://doi.org/10.1016/j.ocemod.2008.07.006</li> <li>Renault, L., McWilliams, J. C., &amp; Penven, P. (2017). Modulation of the Agulhas Current Retroflection and Leakage by Oceanic Current Interaction with the Atmosphere in Coupled Simulations. Journal of Physical Oceanography, 47(8), 2077 - 2100. doi: 10.1175/JPO-D-16-0168.1</li> <li>Renault, L., Molemaker, M. J., Gula, J., Masson, S., &amp; McWilliams, J. C. (2016). Control and Stabilization of the Gulf Stream by Oceanic Current Interaction with the Atmosphere. Journal of Physical Oceanography, 46(11), 3439 - 3453.</li> </ul>
924 925 926 927 928 930 931 932 933 934 935	<ul> <li>Rascle, N., Ardhuin, F., Queffeulou, P., &amp; Croizé-Fillon, D. (2008). A global wave parameter database for geophysical applications. part 1: Wave-current-turbulence interaction parameters for the open ocean based on traditional parameterizations. Ocean Modelling, 25(3), 154-171. doi: https://doi.org/10.1016/j.ocemod.2008.07.006</li> <li>Renault, L., McWilliams, J. C., &amp; Penven, P. (2017). Modulation of the Agulhas Current Retroflection and Leakage by Oceanic Current Interaction with the Atmosphere in Coupled Simulations. Journal of Physical Oceanography, 47(8), 2077 - 2100. doi: 10.1175/JPO-D-16-0168.1</li> <li>Renault, L., Molemaker, M. J., Gula, J., Masson, S., &amp; McWilliams, J. C. (2016). Control and Stabilization of the Gulf Stream by Oceanic Current Interaction with the Atmosphere. Journal of Physical Oceanography, 46(11), 3439 - 3453. doi: 10.1175/JPO-D-16-0115.1</li> </ul>
924 925 926 927 929 930 931 932 933 933 934 935 936	<ul> <li>Rascle, N., Ardhuin, F., Queffeulou, P., &amp; Croizé-Fillon, D. (2008). A global wave parameter database for geophysical applications. part 1: Wave-current-turbulence interaction parameters for the open ocean based on traditional parameterizations. Ocean Modelling, 25(3), 154-171. doi: https://doi.org/10.1016/j.ocemod.2008.07.006</li> <li>Renault, L., McWilliams, J. C., &amp; Penven, P. (2017). Modulation of the Agulhas Current Retroflection and Leakage by Oceanic Current Interaction with the Atmosphere in Coupled Simulations. Journal of Physical Oceanography, 47(8), 2077 - 2100. doi: 10.1175/JPO-D-16-0168.1</li> <li>Renault, L., Molemaker, M. J., Gula, J., Masson, S., &amp; McWilliams, J. C. (2016). Control and Stabilization of the Gulf Stream by Oceanic Current Interaction with the Atmosphere. Journal of Physical Oceanography, 46(11), 3439 - 3453. doi: 10.1175/JPO-D-16-0115.1</li> <li>Rieder, K. F., Smith, J. A., &amp; Weller, R. A. (1994). Observed directional charac-</li> </ul>
924 925 926 927 928 930 931 932 933 934 935	<ul> <li>Rascle, N., Ardhuin, F., Queffeulou, P., &amp; Croizé-Fillon, D. (2008). A global wave parameter database for geophysical applications. part 1: Wave-current-turbulence interaction parameters for the open ocean based on traditional parameterizations. Ocean Modelling, 25(3), 154-171. doi: https://doi.org/10.1016/j.ocemod.2008.07.006</li> <li>Renault, L., McWilliams, J. C., &amp; Penven, P. (2017). Modulation of the Agulhas Current Retroflection and Leakage by Oceanic Current Interaction with the Atmosphere in Coupled Simulations. Journal of Physical Oceanography, 47(8), 2077 - 2100. doi: 10.1175/JPO-D-16-0168.1</li> <li>Renault, L., Molemaker, M. J., Gula, J., Masson, S., &amp; McWilliams, J. C. (2016). Control and Stabilization of the Gulf Stream by Oceanic Current Interaction with the Atmosphere. Journal of Physical Oceanography, 46(11), 3439 - 3453. doi: 10.1175/JPO-D-16-0115.1</li> <li>Rieder, K. F., Smith, J. A., &amp; Weller, R. A. (1994). Observed directional characteristics of the wind, wind stress, and surface waves on the open ocean. Jour-</li> </ul>
924 925 926 927 928 930 931 933 933 933 933 935 936 937	<ul> <li>Rascle, N., Ardhuin, F., Queffeulou, P., &amp; Croizé-Fillon, D. (2008). A global wave parameter database for geophysical applications. part 1: Wave-current-turbulence interaction parameters for the open ocean based on traditional parameterizations. Ocean Modelling, 25(3), 154-171. doi: https://doi.org/10.1016/j.ocemod.2008.07.006</li> <li>Renault, L., McWilliams, J. C., &amp; Penven, P. (2017). Modulation of the Agulhas Current Retroflection and Leakage by Oceanic Current Interaction with the Atmosphere in Coupled Simulations. Journal of Physical Oceanography, 47(8), 2077 - 2100. doi: 10.1175/JPO-D-16-0168.1</li> <li>Renault, L., Molemaker, M. J., Gula, J., Masson, S., &amp; McWilliams, J. C. (2016). Control and Stabilization of the Gulf Stream by Oceanic Current Interaction with the Atmosphere. Journal of Physical Oceanography, 46(11), 3439 - 3453. doi: 10.1175/JPO-D-16-0115.1</li> <li>Rieder, K. F., Smith, J. A., &amp; Weller, R. A. (1994). Observed directional characteristics of the wind, wind stress, and surface waves on the open ocean. Journal of Geophysical Research: Oceans, 99(C11), 22589-22596. doi: https://doi</li> </ul>
924 925 926 927 928 930 931 932 933 934 935 936 937 938 939	<ul> <li>Rascle, N., Ardhuin, F., Queffeulou, P., &amp; Croizé-Fillon, D. (2008). A global wave parameter database for geophysical applications. part 1: Wave-current-turbulence interaction parameters for the open ocean based on traditional parameterizations. Ocean Modelling, 25(3), 154-171. doi: https://doi.org/10.1016/j.ocemod.2008.07.006</li> <li>Renault, L., McWilliams, J. C., &amp; Penven, P. (2017). Modulation of the Agulhas Current Retroflection and Leakage by Oceanic Current Interaction with the Atmosphere in Coupled Simulations. Journal of Physical Oceanography, 47(8), 2077 - 2100. doi: 10.1175/JPO-D-16-0168.1</li> <li>Renault, L., Molemaker, M. J., Gula, J., Masson, S., &amp; McWilliams, J. C. (2016). Control and Stabilization of the Gulf Stream by Oceanic Current Interaction with the Atmosphere. Journal of Physical Oceanography, 46(11), 3439 - 3453. doi: 10.1175/JPO-D-16-0115.1</li> <li>Rieder, K. F., Smith, J. A., &amp; Weller, R. A. (1994). Observed directional characteristics of the wind, wind stress, and surface waves on the open ocean. Journal of Geophysical Research: Oceans, 99(C11), 22589-22596. doi: https://doi.org/10.1029/94JC02215</li> </ul>
924 925 926 927 928 930 931 933 933 933 935 936 937 938	<ul> <li>Rascle, N., Ardhuin, F., Queffeulou, P., &amp; Croizé-Fillon, D. (2008). A global wave parameter database for geophysical applications. part 1: Wave-current-turbulence interaction parameters for the open ocean based on traditional parameterizations. Ocean Modelling, 25(3), 154-171. doi: https://doi.org/10.1016/j.ocemod.2008.07.006</li> <li>Renault, L., McWilliams, J. C., &amp; Penven, P. (2017). Modulation of the Agulhas Current Retroflection and Leakage by Oceanic Current Interaction with the Atmosphere in Coupled Simulations. Journal of Physical Oceanography, 47(8), 2077 - 2100. doi: 10.1175/JPO-D-16-0168.1</li> <li>Renault, L., Molemaker, M. J., Gula, J., Masson, S., &amp; McWilliams, J. C. (2016). Control and Stabilization of the Gulf Stream by Oceanic Current Interaction with the Atmosphere. Journal of Physical Oceanography, 46(11), 3439 - 3453. doi: 10.1175/JPO-D-16-0115.1</li> <li>Rieder, K. F., Smith, J. A., &amp; Weller, R. A. (1994). Observed directional characteristics of the wind, wind stress, and surface waves on the open ocean. Journal of Geophysical Research: Oceans, 99(C11), 22589-22596. doi: https://doi.org/10.1029/94JC02215</li> <li>Rogers, W. E., Babanin, A. V., &amp; Wang, D. W. (2012). Observation-Consistent</li> </ul>
924 925 926 927 929 930 931 932 933 934 935 936 935 936 939 939	<ul> <li>Rascle, N., Ardhuin, F., Queffeulou, P., &amp; Croizé-Fillon, D. (2008). A global wave parameter database for geophysical applications. part 1: Wave-current-turbulence interaction parameters for the open ocean based on traditional parameterizations. Ocean Modelling, 25(3), 154-171. doi: https://doi.org/10.1016/j.ocemod.2008.07.006</li> <li>Renault, L., McWilliams, J. C., &amp; Penven, P. (2017). Modulation of the Agulhas Current Retroflection and Leakage by Oceanic Current Interaction with the Atmosphere in Coupled Simulations. Journal of Physical Oceanography, 47(8), 2077 - 2100. doi: 10.1175/JPO-D-16-0168.1</li> <li>Renault, L., Molemaker, M. J., Gula, J., Masson, S., &amp; McWilliams, J. C. (2016). Control and Stabilization of the Gulf Stream by Oceanic Current Interaction with the Atmosphere. Journal of Physical Oceanography, 46(11), 3439 - 3453. doi: 10.1175/JPO-D-16-0115.1</li> <li>Rieder, K. F., Smith, J. A., &amp; Weller, R. A. (1994). Observed directional characteristics of the wind, wind stress, and surface waves on the open ocean. Journal of Geophysical Research: Oceans, 99(C11), 22589-22596. doi: https://doi.org/10.1029/94JC02215</li> </ul>
924 925 926 927 929 930 931 932 933 934 935 936 937 938 939 940 941	<ul> <li>Rascle, N., Ardhuin, F., Queffeulou, P., &amp; Croizé-Fillon, D. (2008). A global wave parameter database for geophysical applications. part 1: Wave-current-turbulence interaction parameters for the open ocean based on traditional parameterizations. Ocean Modelling, 25(3), 154-171. doi: https://doi.org/10.1016/j.ocemod.2008.07.006</li> <li>Renault, L., McWilliams, J. C., &amp; Penven, P. (2017). Modulation of the Agulhas Current Retroflection and Leakage by Oceanic Current Interaction with the Atmosphere in Coupled Simulations. Journal of Physical Oceanography, 47(8), 2077 - 2100. doi: 10.1175/JPO-D-16-0168.1</li> <li>Renault, L., Molemaker, M. J., Gula, J., Masson, S., &amp; McWilliams, J. C. (2016). Control and Stabilization of the Gulf Stream by Oceanic Current Interaction with the Atmosphere. Journal of Physical Oceanography, 46(11), 3439 - 3453. doi: 10.1175/JPO-D-16-0115.1</li> <li>Rieder, K. F., Smith, J. A., &amp; Weller, R. A. (1994). Observed directional characteristics of the wind, wind stress, and surface waves on the open ocean. Journal of Geophysical Research: Oceans, 99(C11), 22589-22596. doi: https://doi.org/10.1029/94JC02215</li> <li>Rogers, W. E., Babanin, A. V., &amp; Wang, D. W. (2012). Observation-Consistent Input and Whitecapping Dissipation in a Model for Wind-Generated Surface</li> </ul>
924 925 926 927 930 931 932 933 934 935 936 936 938 939 940 941 942	<ul> <li>Rascle, N., Ardhuin, F., Queffeulou, P., &amp; Croizé-Fillon, D. (2008). A global wave parameter database for geophysical applications. part 1: Wave-current-turbulence interaction parameters for the open ocean based on traditional parameterizations. Ocean Modelling, 25(3), 154-171. doi: https://doi.org/10.1016/j.ocemod.2008.07.006</li> <li>Renault, L., McWilliams, J. C., &amp; Penven, P. (2017). Modulation of the Agulhas Current Retroflection and Leakage by Oceanic Current Interaction with the Atmosphere in Coupled Simulations. Journal of Physical Oceanography, 47(8), 2077 - 2100. doi: 10.1175/JPO-D-16-0168.1</li> <li>Renault, L., Molemaker, M. J., Gula, J., Masson, S., &amp; McWilliams, J. C. (2016). Control and Stabilization of the Gulf Stream by Oceanic Current Interaction with the Atmosphere. Journal of Physical Oceanography, 46(11), 3439 - 3453. doi: 10.1175/JPO-D-16-0115.1</li> <li>Rieder, K. F., Smith, J. A., &amp; Weller, R. A. (1994). Observed directional characteristics of the wind, wind stress, and surface waves on the open ocean. Journal of Geophysical Research: Oceans, 99(C11), 22589-22596. doi: https://doi.org/10.1029/94JC02215</li> <li>Rogers, W. E., Babanin, A. V., &amp; Wang, D. W. (2012). Observation-Consistent Input and Whitecapping Dissipation in a Model for Wind-Generated Surface Waves: Description and Simple Calculations. Journal of Atmospheric and Oceanic Technology, 29(9), 1329 - 1346. doi: 10.1175/JTECH-D-11-00092.1</li> <li>Sauvage, C., Lebeaupin Brossier, C., Bouin, MN., &amp; Ducrocq, V. (2020). Charac-</li> </ul>
924 925 926 927 928 930 931 932 933 934 935 936 937 938 939 939 940 941 942 943	<ul> <li>Rascle, N., Ardhuin, F., Queffeulou, P., &amp; Croizé-Fillon, D. (2008). A global wave parameter database for geophysical applications. part 1: Wave-current-turbulence interaction parameters for the open ocean based on traditional parameterizations. Ocean Modelling, 25(3), 154-171. doi: https://doi.org/10.1016/j.ocemod.2008.07.006</li> <li>Renault, L., McWilliams, J. C., &amp; Penven, P. (2017). Modulation of the Agulhas Current Retroflection and Leakage by Oceanic Current Interaction with the Atmosphere in Coupled Simulations. Journal of Physical Oceanography, 47(8), 2077 - 2100. doi: 10.1175/JPO-D-16-0168.1</li> <li>Renault, L., Molemaker, M. J., Gula, J., Masson, S., &amp; McWilliams, J. C. (2016). Control and Stabilization of the Gulf Stream by Oceanic Current Interaction with the Atmosphere. Journal of Physical Oceanography, 46(11), 3439 - 3453. doi: 10.1175/JPO-D-16-0115.1</li> <li>Rieder, K. F., Smith, J. A., &amp; Weller, R. A. (1994). Observed directional characteristics of the wind, wind stress, and surface waves on the open ocean. Journal of Geophysical Research: Oceans, 99(C11), 22589-22596. doi: https://doi.org/10.1029/94JC02215</li> <li>Rogers, W. E., Babanin, A. V., &amp; Wang, D. W. (2012). Observation-Consistent Input and Whitecapping Dissipation in a Model for Wind-Generated Surface Waves: Description and Simple Calculations. Journal of Atmospheric and Oceanic Technology, 29(9), 1329 - 1346. doi: 10.1175/JTECH-D-11-00092.1</li> </ul>
924 925 926 927 928 930 931 933 933 934 935 936 937 938 939 940 941 941 942 944	<ul> <li>Rascle, N., Ardhuin, F., Queffeulou, P., &amp; Croizé-Fillon, D. (2008). A global wave parameter database for geophysical applications. part 1: Wave-current-turbulence interaction parameters for the open ocean based on traditional parameterizations. Ocean Modelling, 25(3), 154-171. doi: https://doi.org/10.1016/j.ocemod.2008.07.006</li> <li>Renault, L., McWilliams, J. C., &amp; Penven, P. (2017). Modulation of the Agulhas Current Retroflection and Leakage by Oceanic Current Interaction with the Atmosphere in Coupled Simulations. Journal of Physical Oceanography, 47(8), 2077 - 2100. doi: 10.1175/JPO-D-16-0168.1</li> <li>Renault, L., Molemaker, M. J., Gula, J., Masson, S., &amp; McWilliams, J. C. (2016). Control and Stabilization of the Gulf Stream by Oceanic Current Interaction with the Atmosphere. Journal of Physical Oceanography, 46(11), 3439 - 3453. doi: 10.1175/JPO-D-16-0115.1</li> <li>Rieder, K. F., Smith, J. A., &amp; Weller, R. A. (1994). Observed directional characteristics of the wind, wind stress, and surface waves on the open ocean. Journal of Geophysical Research: Oceans, 99(C11), 22589-22596. doi: https://doi.org/10.1029/94JC02215</li> <li>Rogers, W. E., Babanin, A. V., &amp; Wang, D. W. (2012). Observation-Consistent Input and Whitecapping Dissipation in a Model for Wind-Generated Surface Waves: Description and Simple Calculations. Journal of Atmospheric and Oceanic Technology, 29(9), 1329 - 1346. doi: 10.1175/JTECH-D-11-00092.1</li> <li>Sauvage, C., Lebeaupin Brossier, C., Bouin, MN., &amp; Ducrocq, V. (2020). Characterization of the air-sea exchange mechanisms during a Mediterranean heavy precipitation event using realistic sea state modelling. Atmos. Chem. Phys.,</li> </ul>
924 925 926 929 930 931 932 933 934 935 936 937 938 939 940 941 942 943 944	<ul> <li>Rascle, N., Ardhuin, F., Queffeulou, P., &amp; Croizé-Fillon, D. (2008). A global wave parameter database for geophysical applications. part 1: Wave-current-turbulence interaction parameters for the open ocean based on traditional parameterizations. Ocean Modelling, 25(3), 154-171. doi: https://doi.org/10.1016/j.ocemod.2008.07.006</li> <li>Renault, L., McWilliams, J. C., &amp; Penven, P. (2017). Modulation of the Agulhas Current Retroflection and Leakage by Oceanic Current Interaction with the Atmosphere in Coupled Simulations. Journal of Physical Oceanography, 47(8), 2077 - 2100. doi: 10.1175/JPO-D-16-0168.1</li> <li>Renault, L., Molemaker, M. J., Gula, J., Masson, S., &amp; McWilliams, J. C. (2016). Control and Stabilization of the Gulf Stream by Oceanic Current Interaction with the Atmosphere. Journal of Physical Oceanography, 46(11), 3439 - 3453. doi: 10.1175/JPO-D-16-0115.1</li> <li>Rieder, K. F., Smith, J. A., &amp; Weller, R. A. (1994). Observed directional characteristics of the wind, wind stress, and surface waves on the open ocean. Journal of Geophysical Research: Oceans, 99(C11), 22589-22596. doi: https://doi.org/10.1029/94JC02215</li> <li>Rogers, W. E., Babanin, A. V., &amp; Wang, D. W. (2012). Observation-Consistent Input and Whitecapping Dissipation in a Model for Wind-Generated Surface Waves: Description and Simple Calculations. Journal of Atmospheric and Oceanic Technology, 29(9), 1329 - 1346. doi: 10.1175/JTECH-D-11-00092.1</li> <li>Sauvage, C., Lebeaupin Brossier, C., Bouin, MN., &amp; Ducrocq, V. (2020). Characterization of the air-sea exchange mechanisms during a Mediterranean heavy precipitation event using realistic sea state modelling. Atmos. Chem. Phys., 20(3), 1675–1699. doi: 10.5194/acp-20-1675-2020</li> </ul>
924 925 926 927 929 930 931 932 933 934 935 936 937 938 939 940 941 942 943 944 945 945	<ul> <li>Rascle, N., Ardhuin, F., Queffeulou, P., &amp; Croizé-Fillon, D. (2008). A global wave parameter database for geophysical applications. part 1: Wave-current-turbulence interaction parameters for the open ocean based on traditional parameterizations. Ocean Modelling, 25(3), 154-171. doi: https://doi.org/10.1016/j.ocemod.2008.07.006</li> <li>Renault, L., McWilliams, J. C., &amp; Penven, P. (2017). Modulation of the Agulhas Current Retroflection and Leakage by Oceanic Current Interaction with the Atmosphere in Coupled Simulations. Journal of Physical Oceanography, 47(8), 2077 - 2100. doi: 10.1175/JPO-D-16-0168.1</li> <li>Renault, L., Molemaker, M. J., Gula, J., Masson, S., &amp; McWilliams, J. C. (2016). Control and Stabilization of the Gulf Stream by Oceanic Current Interaction with the Atmosphere. Journal of Physical Oceanography, 46(11), 3439 - 3453. doi: 10.1175/JPO-D-16-0115.1</li> <li>Rieder, K. F., Smith, J. A., &amp; Weller, R. A. (1994). Observed directional characteristics of the wind, wind stress, and surface waves on the open ocean. Journal of Geophysical Research: Oceans, 99(C11), 22589-22596. doi: https://doi.org/10.1029/94JC02215</li> <li>Rogers, W. E., Babanin, A. V., &amp; Wang, D. W. (2012). Observation-Consistent Input and Whitecapping Dissipation in a Model for Wind-Generated Surface Waves: Description and Simple Calculations. Journal of Atmospheric and Oceanic Technology, 29(9), 1329 - 1346. doi: 10.1175/JTECH-D-11-00092.1</li> <li>Sauvage, C., Lebeaupin Brossier, C., Bouin, MN., &amp; Ducrocq, V. (2020). Characterization of the air-sea exchange mechanisms during a Mediterranean heavy precipitation event using realistic sea state modelling. Atmos. Chem. Phys.,</li> </ul>

951	Climate, 24(5), 1461 - 1479. doi: 10.1175/2010JCLI3718.1
952	Seo, H., Miller, A. J., & Roads, J. O. (2007, feb). The Scripps Coupled
953	Ocean–Atmosphere Regional (SCOAR) Model, with Applications in the
954	Eastern Pacific Sector. Journal of Climate, 20(3), 381–402. doi: 10.1175/
955	jcli4016.1
956	Seo, H., Song, H., O'Neill, L. W., Mazloff, M. R., & Cornuelle, B. D. (2021). Im-
957	pacts of Ocean Currents on the South Indian Ocean Extratropical Storm Track
958	through the Relative Wind Effect. Journal of Climate, $34(22)$ , 9093 - 9113.
959	doi: 10.1175/JCLI-D-21-0142.1
960	Seo, H., Subramanian, A. C., Song, H., & Chowdary, J. S. (2019). Coupled effects of
961	ocean current on wind stress in the bay of bengal: Eddy energetics and upper
962	ocean stratification. Deep Sea Research Part II: Topical Studies in Oceanogra-
963	phy, 168, 104617. (Atmosphere-Ocean Dynamics of Bay of Bengal - Volume I)
964	doi: https://doi.org/10.1016/j.dsr2.2019.07.005
965	Shchepetkin, A. F., & McWilliams, J. C. (2005). The regional oceanic modeling
966	system (ROMS): a split-explicit, free-surface, topography-following-coordinate
967	oceanic model. Ocean Modelling, 9(4), 347-404. doi: https://doi.org/10.1016/
968	j.ocemod.2004.08.002
969	Shin, H. H., Hong, SY., & Dudhia, J. (2012). Impacts of the Lowest Model
970	Level Height on the Performance of Planetary Boundary Layer Parame-
971	terizations. Monthly Weather Review, $140(2)$ , 664 - 682. doi: 10.1175/
972	MWR-D-11-00027.1
973	Skamarock, W. C., Klemp, J. B., Dudhia, J., Gill, D. O., Barker, D., Duda, M. G.,
974	& Powers, J. G. (2008). A Description of the Advanced Research WRF Version
975	3 (Tech. Rep. Nos. NCAR/TN-475+STR). doi: 10.5065/D68S4MVH
976	Smedman, A., Högström, U., Sahleé, E., Drennan, W. M., Kahma, K. K., Petters-
977	son, H., & Zhang, F. (2009). Observational Study of Marine Atmospheric
978	Boundary Layer Characteristics during Swell. Journal of the Atmospheric
979	Sciences, 66(9), 2747 - 2763. doi: 10.1175/2009JAS2952.1
980	Stevens, B., Bony, S., Farrell, D., Ament, F., Blyth, A., Fairall, C., Zöger, M.
981	(2021). EUREC <sup>4</sup> A. Earth System Science Data, $13(8)$ , 4067–4119. doi:
982	10.5194/essd-13-4067-2021
983	Sullivan, P. P., Edson, J. B., Hristov, T., & McWilliams, J. C. (2008). Large-eddy
984	simulations and observations of atmospheric marine boundary layers above
985	nonequilibrium surface waves. Journal of the Atmospheric Sciences, $65(4)$ ,
986	1225 - 1245. doi: 10.1175/2007JAS2427.1
987	Taylor, P. K., & Yelland, M. J. (2001, 02). The Dependence of Sea Surface Rough-
988	ness on the Height and Steepness of the Waves. Journal of Physical Oceanogra-
989	<i>phy</i> , $31(2)$ , 572-590. doi: $10.1175/1520-0485(2001)031(0572:TDOSSR)2.0.CO;$
990	2
991	The WAVEWATCH III Development Group. (2016). User manual and system
992	documentation of WAVEWATCH III version 5.16 (Tech. Rep. No. 329).
993	College Park, MD, USA: NOAA/NWS/NCEP/MMAB. Retrieved from
994	https://polar.ncep.noaa.gov/waves/wavewatch/manual.v5.16.pdf
995	Thompson, E., Fairall, C., Pezoa, S., & Bariteau, L. (2021). ATOMIC ship nav-
996	igation, meteorology, seawater, fluxes: Near-surface meteorology, air-sea
997	fluxes, surface ocean waves, and near surface ocean parameters (tempera-
998	ture, salinity, currents) and primary dataset of ship location and navigation
999	estimated from in-situ and remote sensing instruments aboard NOAA Ship
1000	Ronald H. Brown in the North Atlantic Ocean, near Barbados: Atlantic
1001	Tradewind Ocean-Atmosphere Mesoscale Interaction Campaign 2020-01-
1002	09 to 2020-02-12 (NCEI Accession 0225427). NOAA National Centers for
1003	Environmental Information. Dataset. (Accessed 23 December 2021) doi:
1004	https://doi.org/10.25921/etxb-ht19
1005	Thomson, J. (2012). Wave Breaking Dissipation Observed with "SWIFT" Drifters.

1006	Journal of Atmospheric and Oceanic Technology, 29(12), 1866 - 1882. doi: 10
1007	.1175/JTECH-D-12-00018.1
1008	Thomson, J., Moulton, M., de Klerk, A., Talbert, J., Guerra, M., Kastner, S.,
1009	Nylund, S. (2019). A new version of the SWIFT platform for waves,
1010	currents, and turbulence in the ocean surface layer. In 2019 IEEE/OES
1011	Twelfth Current, Waves and Turbulence Measurement (CWTM) (p. 1-7).
1012	doi: 10.1109/CWTM43797.2019.8955299
1013	Thomson, J., Thompson, E., Iyer, S., Drushka, K., & de Klerk, A. (2021). ATOMIC
1014	SWIFT drifters: Near-surface meteorology, air-sea fluxes, surface ocean waves,
1015	and near-surface ocean properties (turbulent dissipation rate, currents, tem-
1016	perature, salinity) estimated from in-situ and remote sensing instruments
1017	aboard six SWIFT drifters (Surface Wave Instrument Float with Tracking)
1018	launched and recovered for two different deployments from NOAA Ship
1019	Ronald H. Brown in the North Atlantic Ocean, near Barbados: Atlantic
1020	Tradewind Ocean-Atmosphere Mesoscale Interaction Campaign 2020-01-
1021	14 to 2020-02-11 (NCEI Accession 0225279). NOAA National Centers for
1022	Environmental Information. Dataset. (Accessed 23 December 2021) doi:
1023	https://doi.org/10.25921/s5d7-tc07
1024	Tolman, H. L., Balasubramaniyan, B., Burroughs, L. D., Chalikov, D. V., Chao,
1025	Y. Y., Chen, H. S., & Gerald, V. M. (2002). Development and Implemen-
1026	tation of Wind-Generated Ocean Surface Wave Modelsat NCEP. Weather
1027	and Forecasting, $17(2)$ , $311 - 333$ . doi: $10.1175/1520-0434(2002)017(0311)$ :
1028	DAIOWG > 2.0.CO;2
1029	Villas Bôas, A. B., & Young, W. R. (2020). Directional diffusion of surface gravity
1030	wave action by ocean macroturbulence. Journal of Fluid Mechanics, 890, R3.
1031	doi: 10.1017/jfm.2020.116
1032	Wunsch, C. (1998). The Work Done by the Wind on the Oceanic General Circu-
1033	lation. Journal of Physical Oceanography, 28(11), 2332 - 2340. doi: 10.1175/
1034	$1520\text{-}0485(1998)028\langle 2332\text{:}\mathrm{TWDBTW}\rangle 2.0.\mathrm{CO};2$
1035	Zheng, Y., Alapaty, K., Herwehe, J. A., Genio, A. D. D., & Niyogi, D. (2016). Im-
1036	proving High-Resolution Weather Forecasts Using the Weather Research and
1037	Forecasting (WRF) Model with an Updated Kain–Fritsch Scheme. Monthly
1038	Weather Review, 144(3), 833 - 860. doi: 10.1175/MWR-D-15-0005.1
1039	Zou, Z., Song, J., Li, P., Huang, J., Zhang, J. A., Wan, Z., & Li, S. (2019). Effects
1040	of swell waves on atmospheric boundary layer turbulence: A low wind field
1041	study. Journal of Geophysical Research: Oceans, 124(8), 5671-5685. doi:
1042	https://doi.org/10.1029/2019JC015153